CHALMERS
UNIVERSITY OF TECHNOLOGY

Analysis of Static and Dynamic GNSS Multipath in Rural Area

Master's thesis in Communication Engineering

Sepehr Behzadi

DEPARTMENT OF SPACE, EARTH AND ENVIRONMENT

CHALMERS UNIVERSITY OF TECHNOLOGY
Gothenburg, Sweden 2024
www.chalmers.se

Master's thesis 2024

Analysis of Static and Dynamic GNSS Multipath in Rural Area

SEPEHR BEHZADI

CHALMERS
UNIVERSITY OF TECHNOLOGY

Department of Space, Earth and Environment
Division of Geoscience and Remote Sensing
Space Geodesy and Geodynamics
Chalmers University of Technology
Gothenburg, Sweden 2024

Analysis of GNSS Multipath in Rural area
With the help of carrier phase residuals
SEPEHR BEHZADI

Supervisor: : Jan Johansson, Department of Space, Earth and Environment
Examiner: : Jan Johansson, Department of Space, Earth and Environment

Master's Thesis 2024
Department of Space, Earth and Environment
Division of Geoscience and Remote Sensing
Space Geodesy and Geodynamics
Chalmers University of Technology
SE-412 96 Gothenburg
Telephone +46 31 772 1000

Cover:

Typeset in LaTeX
Printed by Chalmers Reproservice
Gothenburg, Sweden 2024

Hereby I certify to be the original author of this report and that it has been designed exclusively by me. In case external information or work has been used, e.g. in form of figures, equations and ideas by other people, this is cited and clearly documented in the text. (Gothenburg, 2024-01-07, Sepehr Behzadi)

Abstract

Presently, the development of autonomous vehicles, particularly in construction, focuses extensively on excavators. This thesis examines the impact of multipath and environmental factors on GNSS signals when a single GNSS antenna is mounted on an excavator. Signal Strength Indicator(SSI) data for Galileo and GPS, alongside GPS carrier phase residuals from the multi-GNSS PPP software GipsyX, were utilized to analyze the environment's influence and the effects stemming from the excavator and its arm orientation. The experiment took place at a farm near the Onsala Space Observatory, involving the daily rotation of the excavator's arm in different directions and simulated digging scenarios.

Analysis of GPS SSI data from RINEX files and GPS post-fit residuals unveiled a systematic effect associated with the excavator's arm orientation. The discernible impact on SSI suggests the potential for predicting the arm's orientation even before data processing. Furthermore, employing residuals enables modeling of effects and errors linked to diverse arm orientations, promising enhanced data processing accuracy. Notably, superior performance was achieved using the L2L signal, demonstrating higher correlations among residuals with matching arm orientations. Using the L2L signal also yielded improved repeatability in position estimations. The study suggests that concurrent consideration of RMSE values and correlation coefficients of SSIs and residuals could effectively forecast the arm's orientation. The measurements were done in a rather simple rural area with few objects, modelling the effects and errors linked to various arm orientations in this kind of area holds promise for enhancing position estimation, both in the same kind of area and as well in more complex areas like cities with numerous reflective objects causing multipath effects or signal blockage.

Keywords: Excavator, GNSS, Rinex, PPP, GipsyX, Signal strength indicator, carrier phase residuals, multipath.

Acknowledgements

I would like to thank my supervisor and examiner Jan Johansson for his support and guidance throughout the project. I would also like thank my family and friends who has given me invaluable support throughout my long educational years at Chalmers, I would like to especially thank my mom and Mr. Shahin Ahmandi (known as Shahin Shawoa).

Sepehr Behzadi, Gothenburg, Januari 2024

List of Acronyms

Below is the list of acronyms that have been used throughout this thesis listed in alphabetical order:

BPSK	Binary phase shift keying
BOC	Binary Offset Carrier
C/A	Coarse/acquisition
CDMA	Code Division Multiple Access
ECEF	Earth-centered, Earth-fixed
EM	Electromagnetic
EUV	Extreme Ultraviolet
GLONASS	GLObalnaya NAvigatsionnaya Sputnikovaya Sistema
GNSS	Global Navigation Satellite Systems
GPS	Global Positioning System
IF	Ionosphere-free
IGS	International GNSS Service
ITRF	International Terrestrial Reference Frame
JPL	Jet Propulsion Laboratory
KF	Kalman Filter
LHCP	Left-Hand Circularly Polarized
LOS	Line of sight
MCS	Master Control Station
NLOS	Non-line of sight
PPP	Precise Point Positioning
RAAN	Right Ascension of the Ascending Node
RHCP	Right-Hand Circularly Polarized
RINEX	Receiver Independent Exchange Format
TEC	Total electron content

Contents

List of Figures

List of Tables

1
Introduction

Throughout history, humans have migrated from one place to another for different reasons, just like animals who have seasonal migration. The difference is that animals know inherently how to navigate their destination [1]. It is important to accurately know the position of point A and B in order to navigate smartly between them so humans have attempted to develop different and effective navigating and positioning techniques under centuries. Our ancestors used celestial observation to determine both time and position on earth for example determining north direction with help of the Pole star in northern hemisphere. All these attempts led to the birth of the Global Navigation Satellite Systems, (GNSS). Many countries have developed their own GNSS, such as the European Galileo and the Chinese BeiDou. Among these systems, Global positioning system (GPS) is the first fully operational GNSS system.
In GNSS, positioning is based on trilateration which means that the receiver estimates its position by measuring its distance from three satellites at the known position. Receiver is able to measure these distances by the help of the signals coming from the satellites in the form of electromagnetic waves. In reality measurements from at least four satellites are needed because the satellite and receiver's clock are note synchronized.
GNSS measurements are not free from errors. It is necessary to compensate these errors for achieving accurate results. Some important error sources are atmospheric errors like Ionospheric delay, Tropospheric delay and attenuation of the signal, Receiver noise and clock instability, errors in satellite ephemeris and etc. The geometries of the visible satellites will also effect the quality and accuracy of the measurements.
One of the most important error sources is multipath. It means that replicas of the original signal can be received due to the reflection phenomena. Materials such as water, glass and metal are good reflector for GNSS signals and can produce strong reflections. It is possible to identify and remove most of the errors by post-processing GNSS data but in autonomous driving is important to do the positioning in real time.

Now a days various efforts are being made in developing autonomous vehicles specially in the field of construction. In an interview on gpswolrd.com [10], it is mentioned that, in many parts of the world, excavators are the prime focus for automation.
In this thesis multipath and surrounding environment's effect on the GNSS signal are in focus when the GNSS antenna is mounted on an excavator. It is common to use dual-antenna GNSS on excavators and this would provide not only position,

but orientation and heading [10]. This project is done by only one GNSS antenna mounted on the excavator. The goal is to identify the multi-path effects and also examine weather it is possible to estimate the orientation of the excavator's arm with only one antenna or not.
Precise point positioning (PPP) is one method used in stand alone GNSS to deal with the measurements' error and reaching decimeter level accuracy. Due to high accuracy this method has been used in this project. In PPP accurate information about satellite orbits and clock collects typically from International GNSS Service (IGS). This orbit and clock products are accurate to within 5 cm.

2

Theory

2.1 GPS

In this report, the main GNSS data used is from the GPS service. Since GPS service is used, the GPS system architecture is briefly described in this section. GPS has three main segments: Space Segment, Control Segment and User segment (see Figure 2.1). The GPS Space and Control Segment are operated by The U.S. Space Force [2].

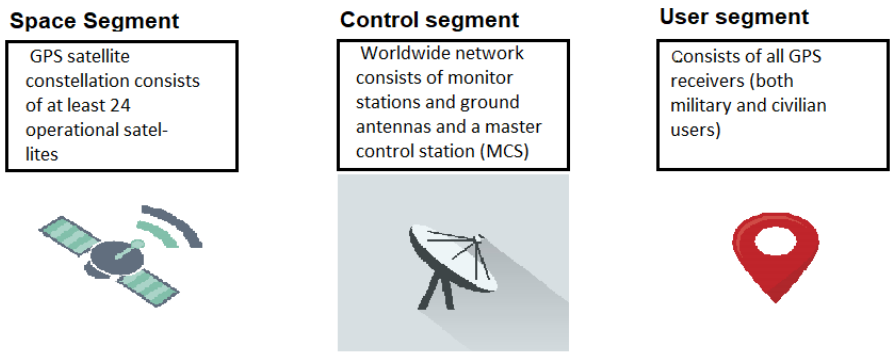

Figure 2.1: Three segments of GPS: Space Segment , Control Segment and User segment [12]

Space Segment: consists of the GPS satellite constellation, comprising 31 operational satellites (as of July 3, 2023) that orbit the Earth within six Earth-centered orbital planes (labeled A to F), with a minimum of four satellites in each plane. These satellites orbit the Earth with a period of half a sidereal day. This is equal to 11 hours 58 minutes. They transmit signals encoded with pseudo-random noise (PRN) codes to the Earth. This enables GPS users to estimate their position by performing ranging measurements. These nearly circular orbital planes are evenly

spaced at 60° intervals, with an inclination angle of 55° relative to the equatorial plane. The point at which each satellite's orbit intersects the equatorial plane during its northward travel is referred to as the Right Ascension of the Ascending Node (RAAN). The positioning of orbital planes is defined with respect to the RAAN, while the satellite's location within the orbital plane is determined by celestial latitude [7]. Figure 2.2 shows the GPS constellation arrangement.

Control segment: comprises of a global network of monitoring stations, ground antennas, and a central command station known as the Master Control Station (MCS). The MCS is located at Schriever Air Force Base in Colorado. The whole GPS network is operated and controlled from the MCS. The control segment is responsible for monitoring satellite orbits, maintaining the health of satellites, issuing commands for minor satellite maneuvers to ensure orbital stability, and orchestrating satellite relocations to address any necessary adjustments in the event of failures [2].

User segment: includes all GPS receivers, serving both military and civilian users. These receivers are designed to accurately determine and deliver position, velocity, and time information. They may take the form of portable, hand-held devices or be installed on various types of vehicles, such as aircraft, ships, and automobiles [2].

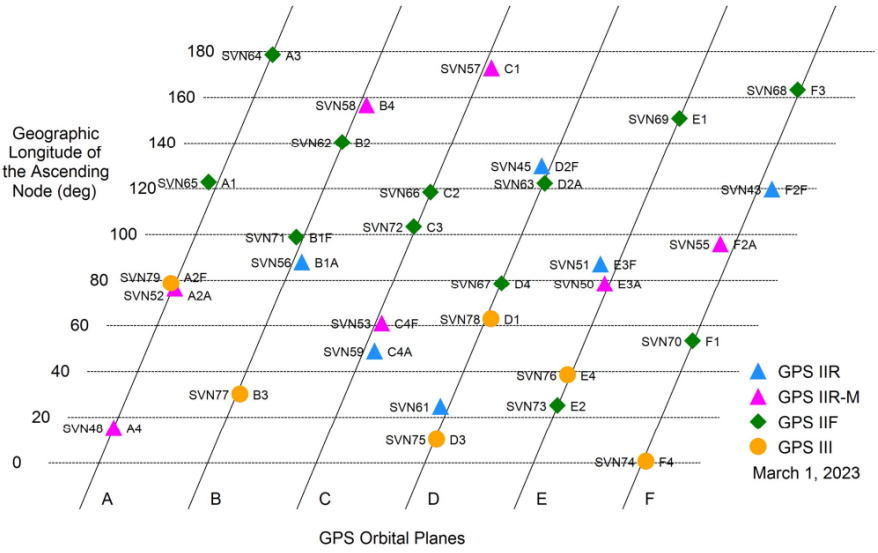

Figure 2.2: The GPS constellation orchestration. 31 operational satellites, which orbit the Earth within six earth-centered orbital planes designated as A through F. Each of these orbital planes is equipped with a minimum of four satellites. Various generations of GPS satellites in this Figure are distinguished by the use of different shapes (circles, squares, and triangles) and colors. This image has been published by the Navigation Center of the United States Coast Guard, a part of the U.S. Department of Homeland Security, available at [12].

2.2 GPS Signals

GPS satellites transmit navigation signals. These signals consist of complex, modulated electromagnetic(EM) waves at radio frequencies. These EM waves possessing four main characteristics: amplitude, phase, frequency, and polarization. These parameters can be modulated to carry information within the signal [11].

2.2.1 GPS signals characteristics

GPS satellites transmit signals on two carrier frequencies within the L-band, referred to as L1 and L2. The fundamental frequency of these signals, $f_0 = 10.23$ MHz , is precisely maintained by rubidium or cesium atomic clocks aboard the satellites. Specifically $f_{L1} = 1575.42$ MHz $= 154 \times f_0$ and $f_{L2} = 1227.6$ MHz $= 120 \times f_0$. The selection of dual frequencies separated by several hundred MHz allows the receiver to estimate signal delays caused by the ionosphere [8]. It is worth noting that, in order to compensate for relativistic effects, the nominal fundamental frequency f_0 is intentionally reduced by approximately 0.005 Hz [14].

GPS signals are right-hand circularly polarized (RHCP).This kind of polarization is used for GPS signal in order to avoid fading problem associated with Faraday rotation[1] [11]. When GPS signal reaches receiver antenna due to reflection, the polarization of the signal might change from RHCP to left-hand circularly polarized (LHCP)[13].

2.2.2 GPS pseudo-random noise (PRN) codes

GPS signals are modulated by codes called pseudo-random noise (PRN). Some of the more relevant PRN code for this thesis are C/A ,L1C , L2C and P(Y).

C/A-codes : coarse/acquisition (C/A) code is the most important signal for mass market applications [17]. It consists of sequence of 1023 binary digits. The period of the C/A Code is about 1 ms which means the generating rate of this code is 1.023 Mbps ($f_0/10$). One chip/bit has the duration of 1 μs and the chip width is about 300 m [11].
Each GPS satellite generates its own unique C/A code. C/A codes belong to the family of Gold codes. These codes have low cross-correlation between all members. When the signals are modulated by these kind of codes the receiver can receive signals simultaneously and easily distinguish them due to the bounded small cross-correlations between them. This technique is known as code division multiple access (CDMA) [16].
32 C/A codes are allocated for the satellites. An additional four unique C/A-codes are available for other uses such as ground transmitters [11]. C/A code was primarily

[1]When a linearly polarized wave travels through a magnetic field in a plasma, such as the ionosphere, its plane of polarization will experience rotation.

Table 2.1: GPS pseudo-random noise (PRN) codes

Parameter 1	C/A-code	P-code	L1C	L2C
Number of bits	1023	2.35×10^{14}	10230	767,250(pilot) + 10230(data)
Chipping rate	1.023 Mbps	10.23 Mbps	1.023 Mbps	1.023 Mbps
Chip width	300 m	30 m	300 m	300 m
One chip duration	1 μs	0.1 μs	1 μs	1 μs
Period	1 ms	266 days	10 ms	L2C-M 20 ms & L2C-L 1.5 s
Frequency band	L1	L1 & L2	L1	L2

thought for acquisition of the P (or Y). The C/A code is used by the receivers both for identification of the space vehicle and also for measuring the time of propagation and computing the range [17].

P-Code: P stands for 'precision'. P code chip width is only 30 m (compare to C/A code with 300 m chip width). This shorter wavelength improves the precision in range measurement. Chip rate of P code is 10.23 MHz (the same as f_0). This code is modulo-2 sum of two other pseudorandom codes and is extremely large. Its pattern does not repeat itself until after 266 days ($2.35 * 10^{14}$ chips). A unique portion of the P-code is assigned weekly to each satellite [11].
P-code is modulated both on L1 and L2. This code is encrypted, so it can be utilized only by authorized users. These users have the advantage of correcting the ionospheric effects on the signals by means of dual-frequency measurements [16].

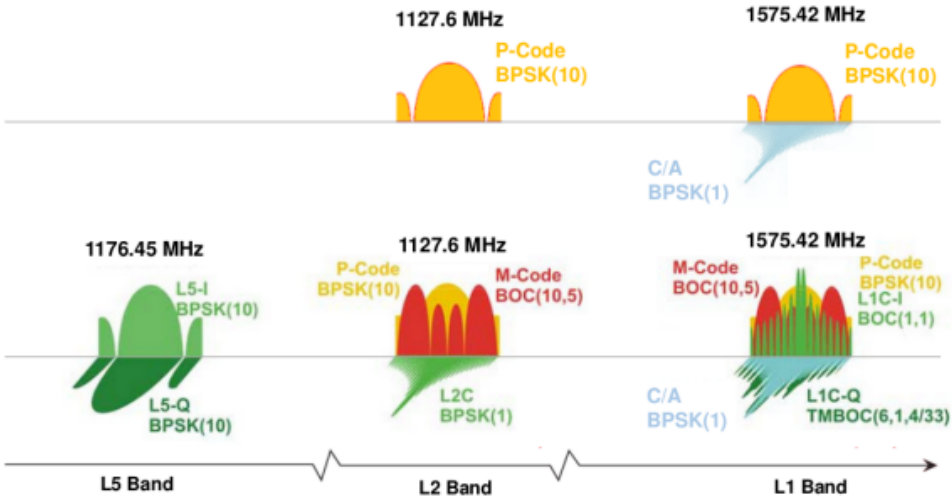

Figure 2.3: GPS Signals frequency spectrum, codes and modulation techniques , Source : GNSS Data Processing, Volume I: Fundamentals and Algorithms [3].

L1C: This is the new civil signal on L1. It shares the same length and frequency as the C/A code but incorporates advanced design which improves its performance. L1C consists of two components a pilot signal and data message [17]. On June 2004 US and EU made an agreement to produce an interoperable signal between GPS and Galileo. As a result of this agreement, L1C was introduced. The modulation format of L1C differs from all other GPS signals but is similar to Galileo's E1 [17][18].

L2C: This is the new modernized civil signal on L2 comprises two PRN ranging codes: the L2 Civil Moderate (L2C-M) code and the L2 Civil Long (L2C-L) code. L2C-L serves as the pilot signal and has a duration of 1.5 seconds, while L2C-M forms the data component of the signal with a duration of 20 milliseconds. These two signal will be time multiplexed, resulting in a composite signal with a chipping rate of 1.023 MHz. The L2C signal enables the use of dual-frequency solutions even for non-authorized users with no access to the P-code [17].
Compared to the L1 C/A signal, this signal offers a higher effective power level and also has more robust cross-correlation properties, which facilitate reception even in challenging environments, such as under trees and indoors [3].

2.2.3 GPS data stream

GPS signals carry Navigation data, which includes information such as ephemeris (the orbital data of the satellite), clock bias parameters, satellite health status, the expected accuracy of range measurements, and an almanac that provides low-resolution ephemeris data for all other GPS satellites. The receiver uses the almanac to quickly lock onto signals from visible satellites that it hasn't yet tracked.

The Navigation message and the PRN code are combined using modulo-2 addition. Subsequently, they are superimposed on both L1 and L2 carriers. This superposition enables the receiver to estimate the duration of signal propagation and position of the satellites [11].

The GPS data stream, resulting from the modulo-2 addition of PRN to the Navigation message, is imposed on the carrier waves using various modulation techniques, including binary phase shift keying (BPSK) and Binary Offset Carrier (BOC). BOC modulation is claimed to have greater resistance to short-range multipath and a slight advantage in code tracking accuracy [19]. Figure 2.3 shows all GPS signals together with their carrier frequency and used modulation technique.

2.3 Range-Based Positioning

As previously stated in the introduction, GNSS positioning is based on ranging which means the location of the receiver is estimated by measuring its distance to a number of satellites at known locations. Upon receiving a satellite signal, a GNSS receiver measures the signal's propagation time from the satellite antenna to

the receiver antenna. By multiplying this time by the speed of propagation and making necessary corrections, the receiver calculates its distance from the satellite. Through a single measurement, the receiver determines its location on a sphere, centered on the satellite, with a radius equal to the measured range denoted as ρ_r^1 (where subscript r refers to the receiver and superscript number denote the satellite). With two simultaneous measurements, the receiver's location is narrowed down to a circle, the intersection of two spheres centered at each satellite, each having a radius equal to the respective measured range ρ_r^1 and ρ_r^2. Upon adding a third simultaneous range measurement ρ_r^3, the potential receiver location reduces from a circle to just two points. One of these points, located far out in space, can be easily eliminated. This process is known as trilateration. If (x_r, y_r, z_r) denotes the receiver location we can write these range equations as :

$$\rho_r^1 = \sqrt{(x_r - x^1)^2 + (y_r - y^1)^2 + (z_r - z^1)^2} \tag{2.1}$$

$$\rho_r^2 = \sqrt{(x_r - x^2)^2 + (y_r - y^2)^2 + (z_r - z^2)^2} \tag{2.2}$$

$$\rho_r^3 = \sqrt{(x_r - x^3)^2 + (y_r - y^3)^2 + (z_r - z^3)^2} \tag{2.3}$$

The unknowns here are the receiver coordinates and as can be seen in the above equations the ranges are non-linear function of the receiver coordinates. By the help of the first-order Taylor polynomial which is the linear approximation we can write:

$$\boldsymbol{p} = \boldsymbol{p_0} + \boldsymbol{A}\boldsymbol{\Delta x} \tag{2.4}$$

Where $\boldsymbol{p}$ is the vector $(\rho_r^1, \rho_r^2, \rho_r^3)^T$, $\boldsymbol{p_0}$ is computed range values based on given satellite coordinates. $\boldsymbol{A}$ is called design matrix and contains partial derivatives of each observation with respect to each parameter. $\boldsymbol{\Delta x} = \boldsymbol{x} - \boldsymbol{x_0}$ is the increment to the initial vector of receiver coordinates that needed to be solved. $\boldsymbol{x} = (x_r, y_r, z_r)^T$ is a vector contains the coordinates of the receiver and $\boldsymbol{x_0} = (x_0, y_0, z_0)^T$ denotes the initial guess of the receiver's position. Note that equations presented in this section are simplified and error sources are not taken into account. Besides determining the receiver's position, other parameters such as receiver clock error and zenith atmospheric delays need to be estimated, requiring at least 4 observations. Note that geometry of the satellite can effect the quality of the solution. This is commonly an overdetermined system, and the best estimation would be found through least-squares or related Kalman filter estimation procedure.

2.4 GPS Observables

GPS has two primary observables: the code pseudorange, measured in meters, and the carrier phase measurement, expressed in cycles. They are used to determine position, velocity and time. Some other observations are Doppler measurements in the unit Hertz and signal strengths [25][11].

In this thesis dataset, signal strength indicator (SSI) were available. SSI is an standardization when the raw signal strength is given in dbHz. The SSI is an

integer ranging from 0 to 9, where 0 signifies blank not known, don't care , 1 is the minimum possible signal strength needs for tracking (Carrier to Noise ratio less than 12 dbHz) , 5 is average/good (30-35 dbHz) and 9 is the maximum possible signal strength ($\geq$ 54 dbHz)[24]. We had no Doppler measurements available.

2.4.1 Code pseudorange

The input signal to the GPS/GNSS receiver is a superposition of signals from different satellites, multipath signals, interferences and noise. Initially the receiver identifies from which satellite the signal has come and then measures travel time of the signal. The time it takes for the signal to travel from the phase centre of the satellite antenna (satellite clock reading at the emission time t_e) to the phase centre of the receiver antenna (the reception time reading at receiver clock t_r). This is accomplished by performing correlation between the GPS signal and internally generated replica of the signal at the receiver. The replica moves in time until the maximum correlation (best matched) is fined [3][14]. Figure 2.4 shows this concept , note that the carrier wave has been removed for simplification.

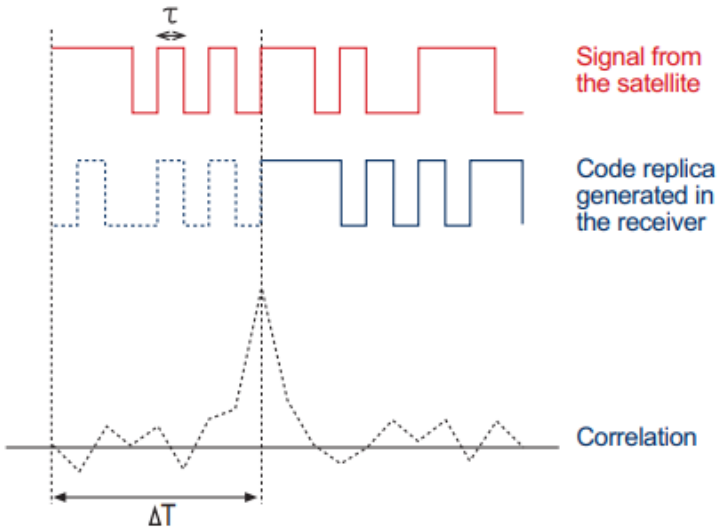

Figure 2.4: Correlation between the GPS signal and the replica in the receiver. Source : GNSS Data Processing, Volume I: Fundamentals and Algorithms [3]

Both t_e and t_r includes biases and errors. The pseudorange can be expressed as :

$$R_r^s = c\Delta t = c((t_r + \delta^r) - (t_e + \delta^s)) = c(t_r - t_e) + c(\delta^r - \delta^s) \tag{2.5}$$

Where c denotes the speed of light, δ^s and δ^r are respective biases in the satellite and receiver clocks. δ^s can be corrected by using clock parameters broadcast by the satellite. R_r^s (subscript r and superscript s denote the receiver and satellite, respectively) represents the pseudorange , theoretically equivalent to the geometric distance in the case of vacuum medium and error-free situation. However as

explained in subsequent section various influences cause R_r^s to deviate from the geometric distance and true range. For this reason it is called pseudorange. The first term in the right hand side of the equation 2.5 $c(t_r - t_e)$ represents the true range and we denote it by ρ_s^r. By using the Pythagorean theorem , this distance can be calculated as $\rho_s^r(t_r, t_e) = \sqrt{(x_s - x_r)^2 + (y_s - y_r)^2 + (z_s - z_r)^2}$ where (x_s, y_s, z_s) is the known satellite coordinate vector provided to the receiver through ephemeris data in the navigation message. (x_r, y_r, z_r) is coordinate vector of the receiver. There are basically four unknown in the equation 2.5 namely (x_r, y_r, z_r and δ^r) (Neglecting the errors). So the receiver would be able to solve for these four unknowns by receiving at least 4 observations from 4 distinct satellites. Considering other correction terms and errors, such as ionospheric effects(δ_{ion}), tropospheric effects(δ_{tro}), Earth tide and ocean loading tide effects (δ_{tide}), multipath (δ_{mul})and relativistic effects (δ_{rel}) along with the residual errors, the equation 2.5 can be redefined as [26] :

$$R_r^s = \rho_s^r(t_r, t_e) + c(\delta_r - \delta^s) + \delta_{ion} + \delta_{tro} + \delta_{tide} + \delta_{mul} + \delta_{rel} + \epsilon \tag{2.6}$$

Here, ϵ denotes the remaining errors. Detailed discussions about certain correction terms will be provided later in the report.

Recent developments have enabled precision up to 0.1% of the chip length for the code pseudorange measurements [14]. This value was traditionaly about 1% of the chip length which means a precision of about 3 m for the the C/A code and 30 cm for the P code [26].

2.4.2 Carrier phase pseudorange

Phase difference between the received and internally generated replica of the signal can also be used to measure the apparent distance between the satellite and the receiver. Receivers that utilize carrier phase measurement can measure the fractional phase difference between the signal and its replica and keep track of phase changes. The beat phase φ_r^s is equal to [14] :

$$\varphi_r^s = \varphi^s - \varphi_r = \Delta\varphi_r^s|_{t_0}^{t_r} + N \tag{2.7}$$

Where φ^s and φ_r are phase of the received signal and reference carrier generated in the receiver respectively at the time of reception t_r, a time epoch reckoned from an initial epoch $t_0 = 0$. φ^s and φ_r are expressed in cycles. Here frequency stability is assumed and deviations of satellite and receiver frequency from the nominal frequency are neglected. N is called integer ambiguity, and is the initial number of full cycles of carrier between satellite and receiver. N is unknown and needed to be resolved, $\Delta\varphi_r^s|_{t_0}^{t_r}$ denotes the fractional phase at epoch t_r augmented by the number of integer cycles since the initial epoch t_0. This can be translated to changes of distance to the satellite . Note that , the initial fractional beat phase $\Delta\varphi_0$ is assumed to be zero for simplicity[14]. $\Delta\varphi_r^s|_{t_0}^{t_r}$ is the only instantaneous and measurable part of beat phase. Phase is related to the range as follows [14] :

$$\varphi^s = ft_r - f\frac{\rho_r^s(t_e, t_r)}{c} - f\delta^s \tag{2.8}$$

$$\varphi_r = ft_r - f\delta_r \tag{2.9}$$

Here f represents the nominal frequency assumed to be the same for both the satellite and the receiver. $\rho_r^s(t_e, t_r)$ denotes the geometric range between the satellite and the receiver. It will be denoted by ρ for simplicity in the upcoming equations. c is the speed of light. δ_r and δ^s are clock errors of the receiver and the satellite, respectively. By substituting equations 2.8 and 2.9 into equation 2.7 , beat phase can be expressed as [14]:

$$\varphi_r^s = ft_r - f\frac{\rho}{c} - f\delta^s - ft_r + f\delta_r = -f\frac{\rho}{c} + f(\delta_r - \delta^s) \tag{2.10}$$

combination of 2.10 and right hand-side of 2.7 gives:

$$\Phi = (-\Delta\varphi_r^s|_{t_0}^{t_r}) = f\frac{\rho}{c} + f(\delta_r - \delta^s) + N \tag{2.11}$$

Φ represents the phase pseudoranges measured in cycles. To convert it to range both sides are multiplied by the wavelength λ. Utilizing the relationship between frequency and wavelength ($f = \frac{c}{\lambda}$), yields [14] :

$$\lambda\Phi = \rho + c(\delta_r - \delta^s) + \lambda N \tag{2.12}$$

This measurement is significantly more precise than the code measurement as the phase of an electromagnetic wave can be measured with accuracy better than 0.01 cycles which corresponds to millimeter precision for GPS/GNSS frequencies [14]. Analogous to equation 2.6 for code measurement, all the correction terms can be added to the equation 2.12 [26] :

$$\lambda\Phi = \rho + c(\delta_r - \delta^s) + \lambda N - \delta_{ion} + \delta_{tro} + \delta_{tide} + \delta_{mul} + \delta_{rel} + \epsilon \tag{2.13}$$

Note that the sign of the ionospheric term here is negative, whereas in equation 2.6 for code measurement model, it is positive. This difference is due to a phenomenon called code-carrier divergence which will be discussed later.
Once the integer ambiguity N is initialized, it will remain constant as long the receiver keeps track of the satellite, in other words the receiver has phase lock on the signal. Loss of the signal lock can occur due to various reasons: obstructions such as trees, buildings, bridges, mountains, etc., or due to low sigal to noise ratio (S/N) owing to adverse ionospheric conditions, multipath, high receiver dynamics, or low satellite elevation or simply due to software failure of the receiver. When signal lock is lost, the ambiguity information is lost too, and N must be reinitialized. This reset would cause a jump in the phase, a phenomenon known as a cycle slip [14].

2.5 Propagations Effects and Error sources

A variety of physical effects introduce errors in GNSS measurements. It is possible to categorize them into three categories: 1) satellite-related errors such as clock error and ephemeris errors; 2) propagation-related errors such as Ionospheric

effects Tropospheric effects; and 3) receiver-related errors including clock error ,multipath,antenna phase center variation and receiver noise. All these errors must be approximated and compensated by using correction terms or some of them can be nearly eliminated using various positioning and design techniques [21].

2.5.1 Clock and Ephemeris Errors

Each GNSS satellite broadcasts information about the bias, drift, and drift rate of its onboard atomic clock via its navigation message. These values are guaranteed to remain almost the same for a long period of time due to high stability of the onboard atomic clock. For GPS specifically, the control segment monitors and updates these parameters every two hours. Using clocks parameters from the navigation message will remove satellite clock error to within $\sim$ 5 ns, on the other hand if the products from IGS is used, this precision would improve further up to $\sim$ 75 ps [21].
Receiver clocks are less stable compare to satellite clocks , they are usually inexpensive quartz clocks. Consequently, receiver clock errors are generally treated as unknown in the observable equations. Alternatively, differencing technique can also be used to remove this error completely [21]. Ephemeris data is also broadcast by the navigation message. It offers an accuracy of $\sim$ 100 cm. More precise and accurate ephemeris data is available from IGS with an accuracy of $\sim$ 2.5 cm. For short baselines, differential positioning can be employed to mitigate errors in ephemeris [21].

2.5.2 Relativistic Effects

Relativity introduces several physical phenomena when there's relative motion between an object and an observer :

- "**Length contraction**: The length of an object moving with some velocity relative to an observer is decreased along the direction of its velocity.
- **Gravitational time dilation**: An object in the presence of a stronger gravitational field will also experience the passage of time more slowly.
- **Motion time dilation**: An object moving relative to an observer will experience the passage of time more slowly than the observer will.
- **Relativity of simultaneity**: Events that appear to occur simultaneously to a stationary observer will appear to occur at different times to an observer with a relative velocity [21]"

These effects intensify as the relative velocity between the object and observer increases. In the case of satellite positioning system ,these effects must be taken into consideration. For instance, in GPS, time dilation effect can cues an accumulated positioning error with the rate of 10 km/day [21].
In GNSS, is common to use Earth-centered, Earth-fixed (ECEF) reference system. This system accommodates the Earth's rotation, allowing receivers to be considered at rest while satellites move at high velocities relative to them. As a result atomic clocks on board experience both motion time dilation and gravitational time dilation due to the present of earth's gravitational field. These effects cues satellite clock to drift $\sim$ -38.6 μs/day . Relativistic effects are considered in designing of satellite

hardware [21].

2.5.3 Atmospheric Effects

As GPS / GNSS signals travel through the Earth's atmosphere their speed and direction of propagation undergo alterations due to interactions with the atoms and molecules of the atmosphere [11]. The Earth's atmosphere can be divided into two distinct regions: the neutral, non-ionized troposphere, and the dispersive ionized ionosphere. Troposphere is actually the name of the the lower part of the Earth's atmosphere. It is mainly composed of dry gases like O_2 and N_2 and water vapors. Its thickness varies from approximately 16 km over the equator to 9 km over the poles. Above the troposphere and below the ionosphere there are some other non-ionized regions namely the stratosphere and the mesosphere. "Tropospheric delay" simply refer to all the delay caused by the non-ionized atmosphere [21]. Figure 2.5 shows different layers of the atmosphere.

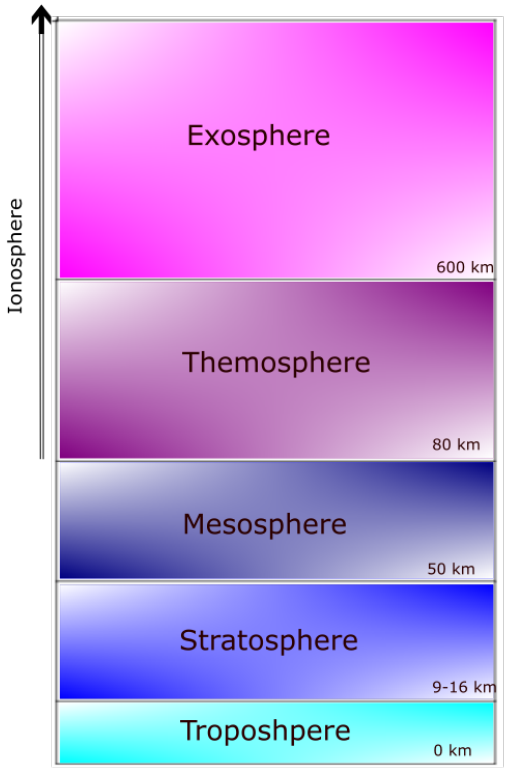

Figure 2.5: Different layers in the Earth's atmosphere.

The signal / EM wave will bend as it travels through the interface of two media with different refractive index or the same medium which has varying refractive index. Refractive index of a medium is defined as $n = \frac{c}{v}$. Where c is the speed of EM wave in a vacuum and v is its speed of propagation in the medium, referred to as phase

velocity. v is related to the wave's angular frequency ω as $v = \frac{\omega}{k}$.Where k is the wave number (cycles per unit distance)[11] :
The change in propagation direction occurs as described by Snell's law[11] :

$$\frac{\sin\theta_i}{\sin\theta_t} = \frac{n_2}{n_1} \tag{2.14}$$

Here n_1 is the refractive index of the first media, n_2 is the refractive index of the second medium, θ_i denotes the incident angle, and θ_t is the transmitted angle [11].

A medium can be dispersive, this means the phase velocity and wave number depend on the wave's frequency in this medium. The carrier and the modulation of the signal can be seen as superposition of waves with different frequencies. In a dispersive medium, the carrier and the modulation of the signal travel with different speeds. The carrier's speed is called phase velocity and propagation speed of the modulation is reffed to as the group velocity [11]. In non-dispersive medium these two velocities are equal[3].

Tropospheric Delay: Troposphere is not a dispersive medium for frequencies up to 15 GHz which includes GPS/GNSS signals. This means both phase and group velocity experience a common delay depending on changes in the refractive index. The effective radio path length, denoted by S, according to Fermat's principle , is given by [21] [3]:

$$S = \int_s n(s)\, ds \tag{2.15}$$

Here n represents the varying refractive index as a function of position s. In the formulation of pseudorange estimation, the path is assumed to be straight line with n=1 constant along the path, which gives [21]:

$$S_0 = \int_{s_0} ds \tag{2.16}$$

Tropospheric delay can be expressed as :

$$\Delta S = S - S_0 = \int_s n(s)\, ds - \int_{s_0} ds = \int_s [n(s) - 1]\, ds + (\int_s ds - \int_{s_0} ds) \tag{2.17}$$

Usually represented as :

$$\Delta S = 10^{-6} \int_s N(s)\, ds + (\int_s ds - \int_{s_0} ds) \tag{2.18}$$

N is called refractivity and is equal to $(n-1) * 10^6$. The second term on the right hand side of the equation 2.18 , $(\int_s ds - \int_{s_0} ds)$ describes the increased path length due to geometric bending of the signal path and is negligible for elevation angles above 5° [21][16]. This effect is less than 3 mm for elevations greater than 20° , about 2 cm for elevations near 10° and about 17 cm for elevations close to 5°. [23]. The refractivity ,N, is summation of hydrostatic(dry) and non-hydrostatic (wet) components as follows :

$$N_{dry} = K_1 \frac{P_d}{T} \tag{2.19}$$

N_{dry} is the hydrostatic component of the total refrectivity, arises from the influence of dry gases such as N2 and O2. T is representing the tropospheric absolute temperature and P_d is partial pressure of dry air. K_1 is the proportionality constant and is determined by experiment [21].

N_{wet} denotes the non-hydrostatic component of the total refrectivity and it comes from the influence of water vapor in the troposphere. Similar to dry gases the refractivity of water vapor can be expressed in terms of partial pressure P_w (of wet air) and tropospheric absolute temperature T:

$$N_{wet} = K_2 \frac{P_w}{T} + K_3 \frac{P_w}{T^2} \tag{2.20}$$

Due to the polar nature of water vapor molecules, their electric dipole reacts differently to incident electromagnetic fields compared to dry gases. That's why N_{wet} has an additional term in its expression. Again K_2 and K_3 are experimentally determined constants [21].
total refractivity of the troposphere can be expressed as summation of the dry and wet components

$$N = N_{dry} + N_{wet} = K_1 \frac{P_d}{T} + K_2 \frac{P_w}{T} + K_3 \frac{P_w}{T^2} \tag{2.21}$$

Smith and Weintraub [22] , shows in their paper that : $K_1 = 77.60 \pm 0.013\, K/mb, K_2 = 71.6 \pm 8.5\, K/mb, K_3 = (3.747 \pm 0.031) * 10^5\, K^2/mb$. Note that in equation 2.21 , it is assumed that both dry gases and water vapor behave as ideal gases. For more precision is possible to add an compressibility factor. This correction addresses deviations in air behavior from that of an ideal gas [11].
The equation 2.18 can be used to estimate tropospheric path delay along any path. This means the delay is dependent on the signal's path length through the troposphere. Signals coming from lower elevation angels will experience greater delay than those from higher angles. As shown in the equation 2.21 N itself depends on atmospheric parameters such as pressure and temperate at any given location and it is not practical to determine these information in all possible locations. A more convenient approach to handle this delay is to use of a mapping functions. These functions relate the zenith path delay to paths at other elevation angles [21].

Ionospheric Delay: Ionosphere is the upper part of the atmosphere as it was illustrated in Figure 2.5. This layer is the most significant error source of GPS/GNSS signals [21]. The border of this layer has defined differently in different literature ,it extents approximately between 70 km up to 1000 km (in some literature up to 2000 km) above the Earth's surface [21]. This layer is characterized by gas molecules being ionized, with a substantial presence of free electrons, primarily resulting from collisions between high-energy solar radiations, like X-rays and Extreme Ultraviolet (EUV) rays, and gas molecules. The abundance of charged particles transforms the

ionosphere into a plasma [21][3].

Ionospheric effects can be categorized into two major groups: effects coming from the total electron content (TEC) along the signal path such as Faraday rotation , group delay and phase advance, and the second group is stochastic effects arising from ionospheric irregularities [21][11].
Using only correction terms from navigation message receiver would be able to remove about half of the error contribution of the ionosphere. This is not sufficient for PPP (precise point positioning). The ionosphere's dispersive nature implies a frequency-dependent change in the refractive index, causing varied induced ionospheric errors across different GNSS observables at distinct frequencies. The ionospheric error term I_i for frequency f_i (i being the frequency index) is approximately [21]:

$$I_i = \frac{40.3}{f_i^2} TEC \tag{2.22}$$

Due to this frequency dependency, 99.9 % of the first-order ionospheric effects can be eliminated using a linear combination of measurements from two different frequencies. Since it is difficult to model and remove ionospheric refraction due to its complexity, PPP computes ionosphere-Free Combination with dual-frequency support [3]. If R_1 and R_2 are pseudorange measurements coming from L1 and L2 frequencies, respectively, then the Ionosphere-free range measurement R_{IF} is given by [21]:

$$R_{IF} = \frac{f_1^2 R_1 - f_2^2 R_2}{f_1^2 - f_2^2} \tag{2.23}$$

As previously mentioned, the ionosphere is a dispersive medium. As a result the group velocity and phase velocity differ within it. The pseudorange measurement which is associated with the modulation of the signal will face a delay which is called group delay. Conversely, the wavefronts of the carrier wave will propagate faster through the ionosphere and this effect is called phase advanced. This phenomenon is known as carrier-code divergence. This is why the sing of ionospheric error for carrier phase measurement is the opposite of the one for pseudorange measurement [21].

2.6 Multipath

The term 'multipath' refers to the situation where the signal transmitted from the satellite arrives at the receiver through several different propagation path. This phenomenon mostly arises due to reflection from surfaces close to the receiver [14] or diffraction at the edges of obstructions [27].
The reflected signals can arrive coherently if the surfaces are smooth relative to the signal wavelength; otherwise, they arrive incoherently. Mostly, multipath effects originate from coherently reflected signals from smooth surfaces, known as specularly reflected signals [28].
The received signal might comprise both the direct signal, referred to as line of sight

(LOS), and an indirect signal, known as non-line of sight (NLOS). Sometimes, only the NLOS signal reaches the receiver antenna [29], termed as shadowing [27]. Shadowing effects arise from reflections, scattering, or signal bending (diffraction) due to obstructions between the transmitter and receiver, leading to power fluctuations in the received signal [30].
Figure 2.6 shows that all NLOS signals travel longer paths compared to the LOS signal. NOLS signals are typically weaker than the direct one [2]. NOLS signals distort the LOS signal and this affects both code and carrier range measurements [2]. However, the signal structure inherently provides some multipath immunity, suppressing the reflected signal during the correlation process when its delay exceeds 1.5 chips. This is due to the C/A code's nearly zero auto-correlation function for delays longer than 1.5 chips (equal to about 500 meters of extra path length for the signal) [2].

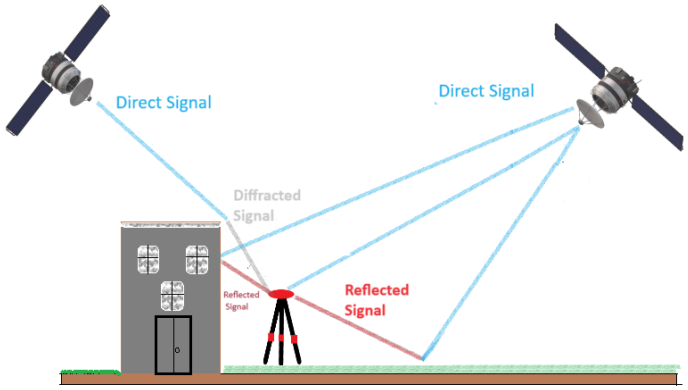

Figure 2.6: Shows different scenarios about how the signal could possibly reach the receiver.

The measurement's error due to multipath, depending on the reflectivity of the environment, is typically between 1-5 m for code range measurement and between 1-5 cm for carrier phase range measurement [2].These values may increase if linear combination of the signals are used [14].
Code range error due to multipath has the dominant effect when both observable are used, especially in applications requiring instantaneous carrier-phase ambiguity resolution.This is because the accuracy of code observations affects the search space for determining integer phase ambiguity. Resolving the integer phase ambiguity will take longer time as the search space gets larger due to errors in the code range measurement caused by multipath [31].

The mulipath effects on the signal can be estimated using a combination of two frequencies. This is due to the fact that the troposphere, clock errors, and relativistic effects are not frequency-depended and and remain consistent across both frequencies. In contrast, ionospheric refraction and multipath vary depending on the signal's frequency. When employing the ionosphere-free combination, all errors

except for multipath are canceled out. Therefore, the residuals, apart from the noise level, reflect the influence of multipath [15]. When the multipath environment remains static the It is possible to use the repeatability of the multipath to distinguish its effect from noise. A GPS satellite repeats its ground track everyday (approximately every 23 h and 56 min). So if the receiver and multipath-producing objects are stationary , then the same error will occur again every day [27].

2.6.1 Reflection characteristics and Fresnel zones

The amplitude of a reflected or diffracted signal is primarily influenced by the reflection coefficient of the reflecting surface. Reflection coefficient itself, is depended on the angel of incidence. It achieves maximum values when the signal is nearly parallel to the surface, notably evident in low-elevation satellite signals reflected from the ground. In the specific case of our study involving an excavator surrounded by a grassy field, the grassy field's reflection coefficient at normal incidence for L1 frequency is 0.334, leading to a signal attenuation of -9.53 dB. Signals from satellites illuminate areas rather than single points, emitted with an aperture angle of $\pm 13.9°$. These active scattering regions, contributing to the reflected signal, are termed Fresnel zones [27]. Following the theory of optics ,If an object span significant fraction of a cross-section of the first Fresnel zone then this object could possibly be a significant signal reflection source [27].

If the receiver antenna is 1 meter high and the satellite is at the zenith, the radius of the Fresnel zone cross-section (the area is a circle in this case) is 0.436 meters for the L1 frequency. For a 5° elevation angle, the length of the semimajor axis of the cross-section is 17 m. When the height of the antenna increases these areas increase as well. With a height increase to 10 meters, the radius of the circular cross-section expands to 1.4 m , and for the 5° elevation angle satellite, the semimajor axis length is approximately 54 m [27]. In any case, in order for an object to be significant source of reflected energy , it needs to be more than a wavelength in size [27].

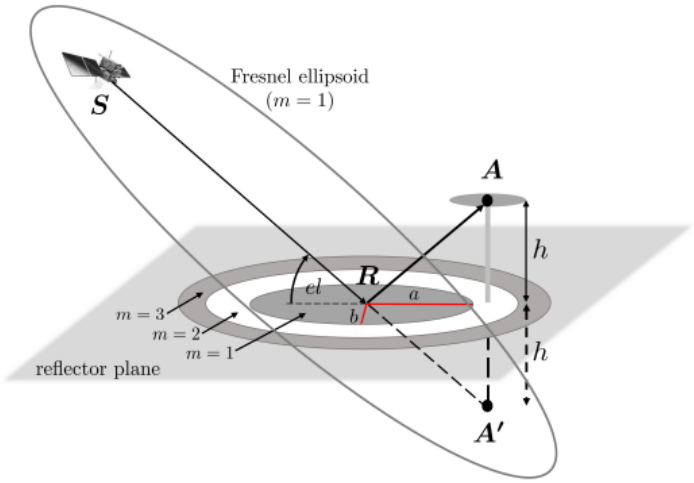

Figure 2.7: Fresnel zones Source : GPS Multipath Analysis Using Fresnel Zones [31]

As previously explained in section 2.2, GPS signals are Right-Hand Circularly Polarized (RHCP). When these signals encounter a perfect conductor, like a metal surface, they undergo a polarization reversal, resulting in a Left-Hand Circularly Polarized (LHCP) reflected signal. On non-perfect conductor surfaces, the reflected signal becomes a mix of RHCP and LHCP, influenced by the Brewster angle. When the incident angle exceeds the Brewster angle, the reflected signal turns LHCP, and vice versa. GNSS antennas are engineered to suppress any polarization other than RHCP [13][27].

3
Methods

Figure 3.1: Placement of the GNSS antenna on the Excavator

3.1 Environment of the experiment

A single GNNS antenna was mounted on an excavator, positioned on top of its cabin behind the arm (refer to Figure 3.1). The excavator was situated in a farm near the Onsala Space Observatory. Figure 3.2 from google maps shows the the exact area of the experiment. The red marker in the image indicates the excavator's placement.The primary objective of the project was to analyze the environmental impact on measurements, particularly investigating the effects of the excavator itself, including the rotation and orientation of its arm. This area was selected for the experiment due to its simplicity (compared to dense city areas with lots of reflectors and signal blockages). It comprises a building, a tree, some rocks and open wide grassy field. The results of this experiment can serve as a foundation for understanding and predicting behaviors in more complex environments. Figure 3.4 shows

this area and these objects.
Tables from [32] outline that, for an antenna with a 2m height from the ground (similar to our setup) and operating at frequency L1, the first Fresnel zone expands approximately between 5m to 30m around the GNSS antenna, depending on the elevation angle.

Figure 3.2: Location of excavator (57°24'04.0"N 11°57'38.9"E)

Figure 3.3 provides a detailed view of the area surrounding the excavator. circle with the radius of approximately 30m around the excavator is marked.
Red dots: Red dots on the circle highlight areas where signals (especially from low-elevation satellites) may encounter blockage or potential diffraction. Positioned to the south of the excavator is a building with wooden walls and a possibly metallic-layered roof. A huge tree is located to north north-east of the excavator which also can attenuate and block the signal.
Light green squares: There are three regions on the circle's area which were marked by light green squares. There are chances for ground reflections from these areas but there is no blockage to the signal.
Blue triangles and dark green squares: For the signals coming from these directions there is possibility that the coming signal reflects from the ground and also from the building and then reaches the GNSS antenna on the excavator.
White dots and orange dots: An area on the left side of the excavator is marked by white dots. Orange dots inside this area representing rocks approximately 3 meters in height. Inside the area, there's a road bordered by rocks on its left side, leading further into a zone populated by trees. Signals from low-elevation satellites might encounter ground reflection from the road and face potential issues of blockage, attenuation, and diffraction due to the presence of surrounding trees and rocks."

Table 3.1: Description of the symbols used in the Figure

Symbol	Description
	ground reflections, no blockage to the signal .....
	Areas where signals may encounter blockage or potential diffraction, Ex. the Building and tree .....
	Reflection from the ground and/or the building .....
	Signals from low-elevation satellites might encounter ground reflection from the road and face potential issues of blockage, attenuation, and diffraction due to the presence of surrounding trees and rocks

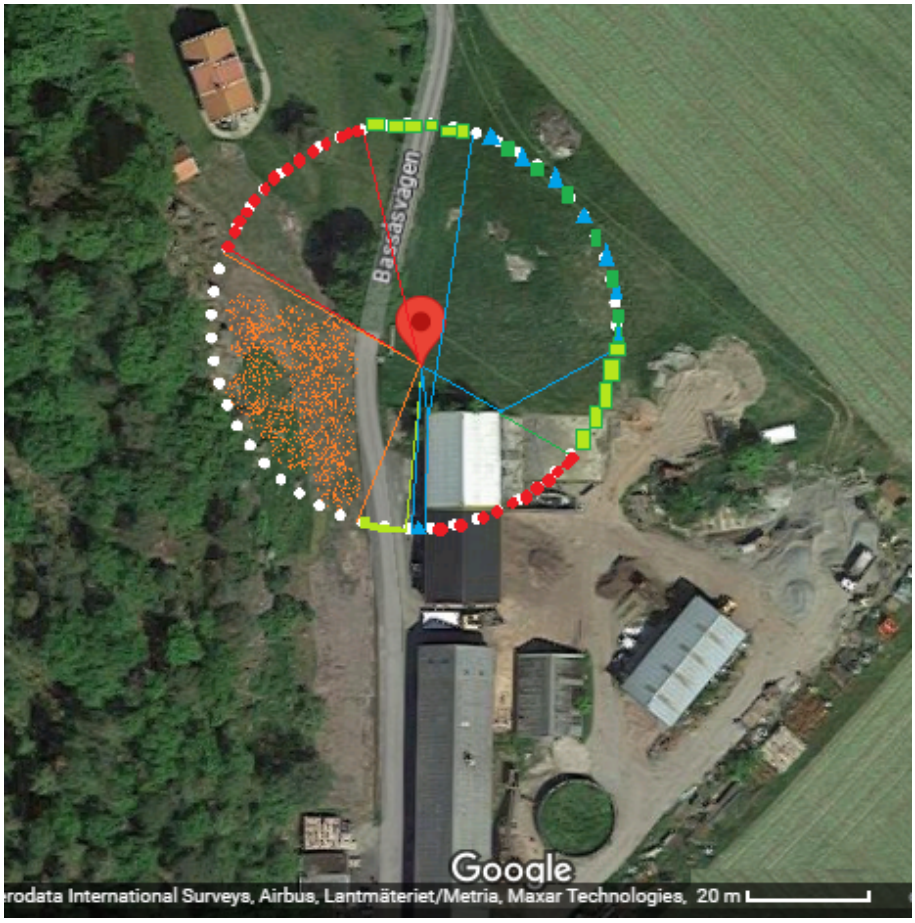

Figure 3.3: preliminary analysis of the excavator's surroundings area

Figure 3.4: surrounding of the excavator

3.2 Equipments

3.2.1 Antenna and Receiver

The antenna used in this project was a Leica AS10 high-precision geodetic one. This antenna supports the GPS, GLONASS, Galileo signals. The receiver used in the project was a multi-frequency GNSS reference called PolaRx5. It provides low-noise measurements with a patented multipath mitigation technology which provides protection against short-delay multipaths [34]. The receiver is fabricated by the Septentrio company. The companies' website claims that the receiver is capable of constantly monitoring and protecting against interference, multipath and other environmental effects. The following pictures show the antenna and the receiver.

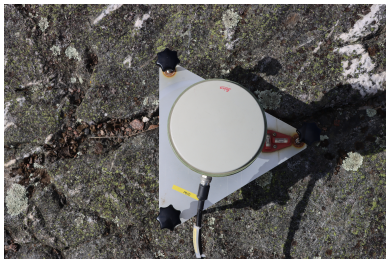

Figure 3.5: Leica AS10 antenna

Figure 3.6: PolaRx5 receiver

3.3 Data Processing

3.3.1 Data formats

The initial output format from the receiver was .tar.gz which is compressed archive file format. The format is a combination of two other archive formats, namely TAR (tape archive) and GZIP. The files were decompressed in Windows. They adopted the CompactRINEX format, also known as the Hatanaka-compressed format for RINEX (Receiver INdependent EXchange) files. Subsequently, these files underwent conversion to RINEX format using the website `https://terras.gsi.go.jp/ja/crx2rnx.html`.
RINEX is an international standard format used by the GNSS receivers in order to store measurements in a standardized way [33].The RINEX version used in this project was 3.04. The RINEX files had two types they were either Observation data file or Navigation message file. Observation files encapsulated code and carrier phase measurements and signal strengths from various GNSS constellations, recorded at one-second intervals. On the other hand, Navigation message files contained essential data about satellites' clocks and orbits. These data were used in this project to find azimuth and elevation of each observation stored in the RINEX files. This was done employing the matlab function "gnssconstellation".
In the subsequent stage, the RINEX files were processed using the GipsyX software. Raw RINEX data was also utilized to analyze multipath effects in this project.

3.3.2 Precise Point Positioning

Until the mid-1990s, almost all geodetic GPS applications used relative baseline positioning which means a secondary observation from a reference station with known position was used to remove errors. In 1997 a new method known as precise point positioning (PPP) was introduced [27]. PPP requires observations only from a single receiver.
PPP makes use of the ionosphere-free (IF) combinations (equation 2.23) of dual-frequency pseudorange and carrier-phase observations to deal with the ionospheric errors. PPP relies on precise corrections for satellite orbits and clock offsets provided by the International GNSS Service (IGS). Note that providing these precise correction information needs a global tracking network. The unknown parameters of a typical PPP model are: receiver position coordinates, receiver clock, zenith troposphere delay and carrier-phase ambiguities. Recalling equation 2.4 the design matrix of PPP solution consists of the partial derivatives with respect to these parameters [27].

3.3.3 Computer software

GipsyX, a GNSS data analysis software utilized in this project, operates in PPP mode for post-processing the data. Developed by NASA Jet Propulsion Laboratory, GipsyX takes RINEX observation files as input. Initially, the software identifies outliers using specific thresholds and then generates ionospheric-free observables

(both for code - P3, and carrier phase - L3 measurements) as explained in Section 2.5.3. Using IGS products, including precise satellite orbits and clocks, alongside external data concerning the receiver, antenna's phase center, and Earth geophysical displacement, GipsyX estimates initial distances between the receiver and satellites. Subsequently, the software calculates the pre-fit residual, representing the difference between Observations (typically labeled "O" in charts) and Computed (typically labeled "C" in charts) values. This pre-fit residual undergoes a Kalman filter process. Output of the filter is a new estimate for the unknown parameters such as receiver position coordinates, receiver clock , zenith troposphere delay and carrier-phase ambiguities.
In essence, the filter relies on Bayesian statistics and conditional probabilities, merging measurements with the current-state estimate via the Kalman gain to produce a new state estimate. The gain assigns weight to the measurements and current-state estimate. The output of this process, known as post-fit residuals, specifically captures unmodeled errors like atmospheric inhomogeneity and site-specific multipaths [35].

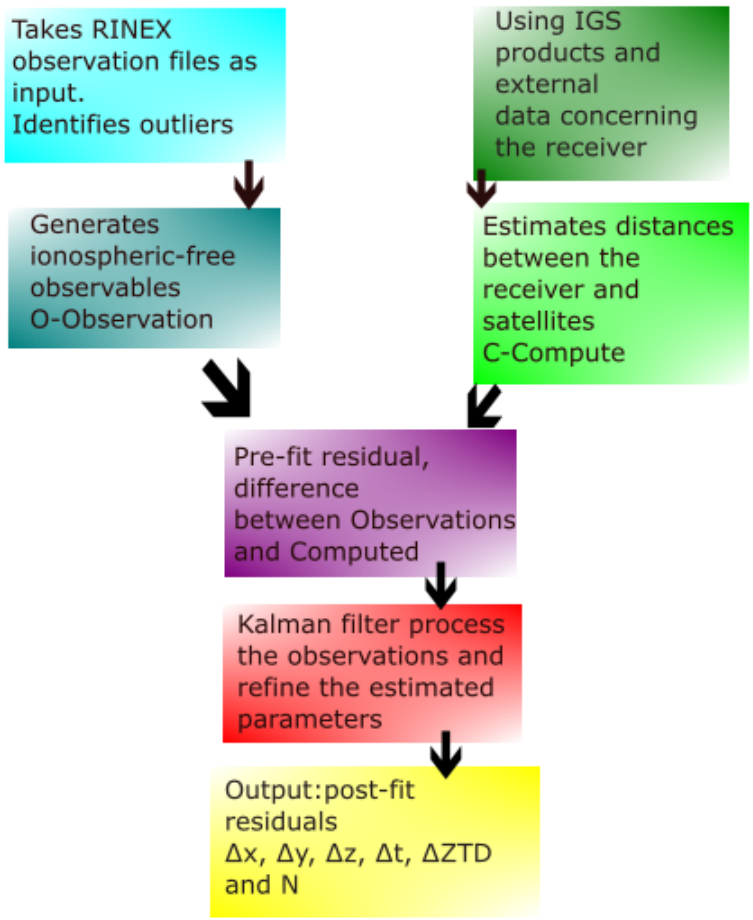

Figure 3.7: Block diagram of the GipsyX processing steps

3.4 Measurements

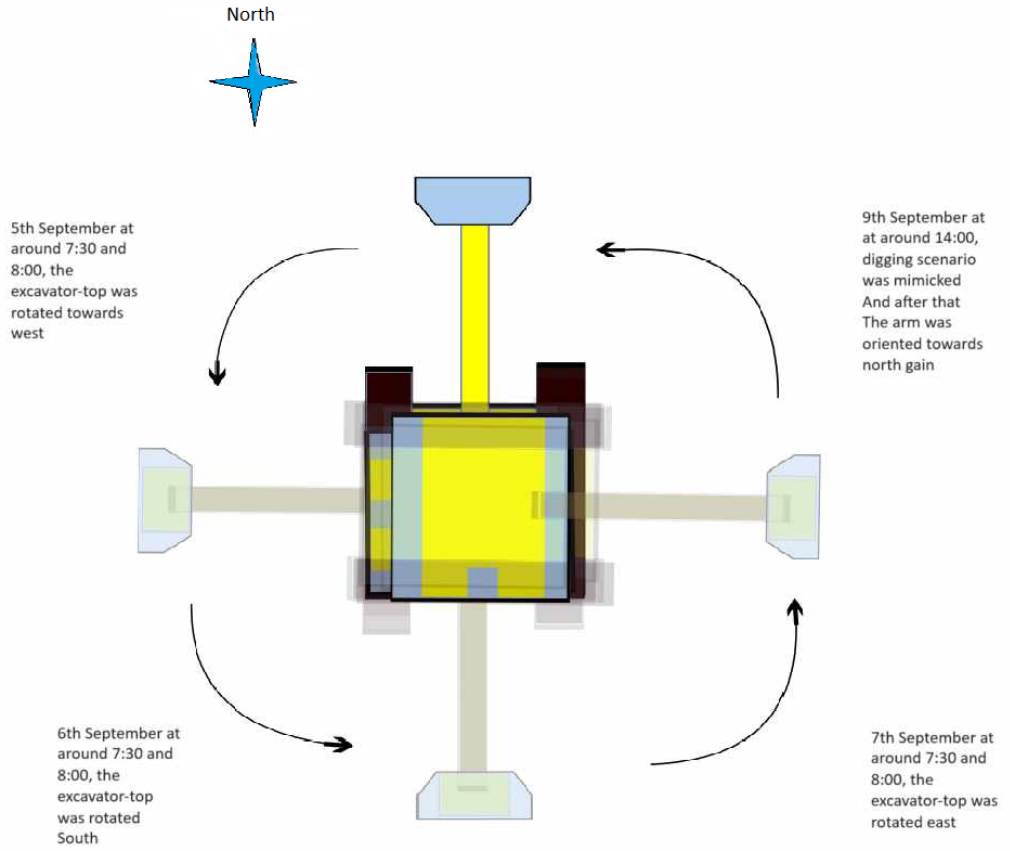

Figure 3.8: Shows orientation and rotation of the excavator's arm on each day

As mentioned earlier, a single GNSS antenna was mounted on an excavator, positioned atop its cabin behind the arm (refer to Figure 3.1). The excavator was situated in a farm near the Onsala Space Observatory. During the experiment, the excavator's arm rotated in various directions each day, and a digging scenarios was also simulated. However, since the antenna wasn't precisely centered on the excavator's cabin, its position changed by approximately half a meter with each rotation. This was taken into account during post-processing to prevent error propagation into the residuals.

3rd September: The antenna was mounted on the excavator, with the arm directed towards the north. The measurements started on this day.

5th September: Between 7:30 and 8:00, the excavator's arm was adjusted to point westward.

6th September: Again around 7:30 to 8:00, the excavator's arm was rotated to point southward.
7th September: Again around 7:30 to 8:00, another 45° rotation was done so the excavator's arm pointed easthward.

This means there exists at-least one day of measurements with antenna pointing north, west, south and east.

9th September: Approximately at 14:00, digging scenario was mimicked.
10th and 11th September: The antenna/excavator remained stationary after the digging scenario. The operator was instructed to leave the excavator in its initial position, likely pointing the arm towards the north again.

The signal strength indicators, Pseudorange, and the number of cycles were recorded for the C1C, L1C, L2W, and L2W channels. These channels were initially selected as they were available for all GPS satellites. As the project progressed, the newer and higher-quality GPS signals, C2L and L2L, were also incorporated, although they weren't available for all GPS satellites. Initially, the project focused solely on GPS signals, but for a more comprehensive analysis, signal strength of one Glonass and two Galileo signals were included in the final phase.

4

Results and discussion

In the following section, the results of the project will be presented. The analysis begins by examining the raw RINEX data collected directly from the receiver, before any processing by GipsyX. Subsequently, the post-fit carrier phase residuals are analyzed, followed by an examination of the position estimations. These pieces of information will be used to explore whether there are any systematic effects specifically caused by the rotation of the excavator's arm and if there is any dependency between the different data and the orientation of the arm.

4.1 Signal Strength Indicator

4.1.1 Galileo's signal strength

Measurements from September 3rd to 11th are available for analysis. The investigation starts with a sky plots displaying Galileo's signal strength for three distinct signals: C1C (frequency: 1575.42 MHz), C6C (frequency: 1278.75 MHz), and CQ7 (frequency: 1207.140 MHz). Refer to Figure 4.1 for the sky plots, illustrating the mean value of the Signal Strength Indicator (SSI) in the left column and the standard deviation (std) in the right column. All measurements from each day were combined and analyzed collectively. The Galileo Constellation's ground track extensively covers the excavator's surrounding area, making it an ideal candidate for an initial investigation into the environmental impact on the signal.

The mean and standard deviation were calculated within a cell area expanding 5^o in azimuth and 2.5^o in elevation. This resolution was chosen through iterative testing, aiming to maintain data variations while reducing noise to generate a smooth sky plot. Subsequently, the entire sky map is divided into a grid of cells, with each cell associated with calculated mean and standard deviation values. This resolution for cell has been applied throughout this project unless specified otherwise. This simplifies all subsequent comparisons and calculations.

Galileo's SSI maps in the figure 4.1 aligns fairly well with the preliminary study of the excavator's surroundings (refer to Figure 3.3). Notably, the impact of the tree is prominently visible in the azimuth range of 300^o to 360^o, exhibiting notably low strength across all signals and high standard deviation. The signal CQ7, with the lowest frequency, displays the highest strength in the presence of the tree. This is due to its increased penetration resulting from its shorter wavelength.

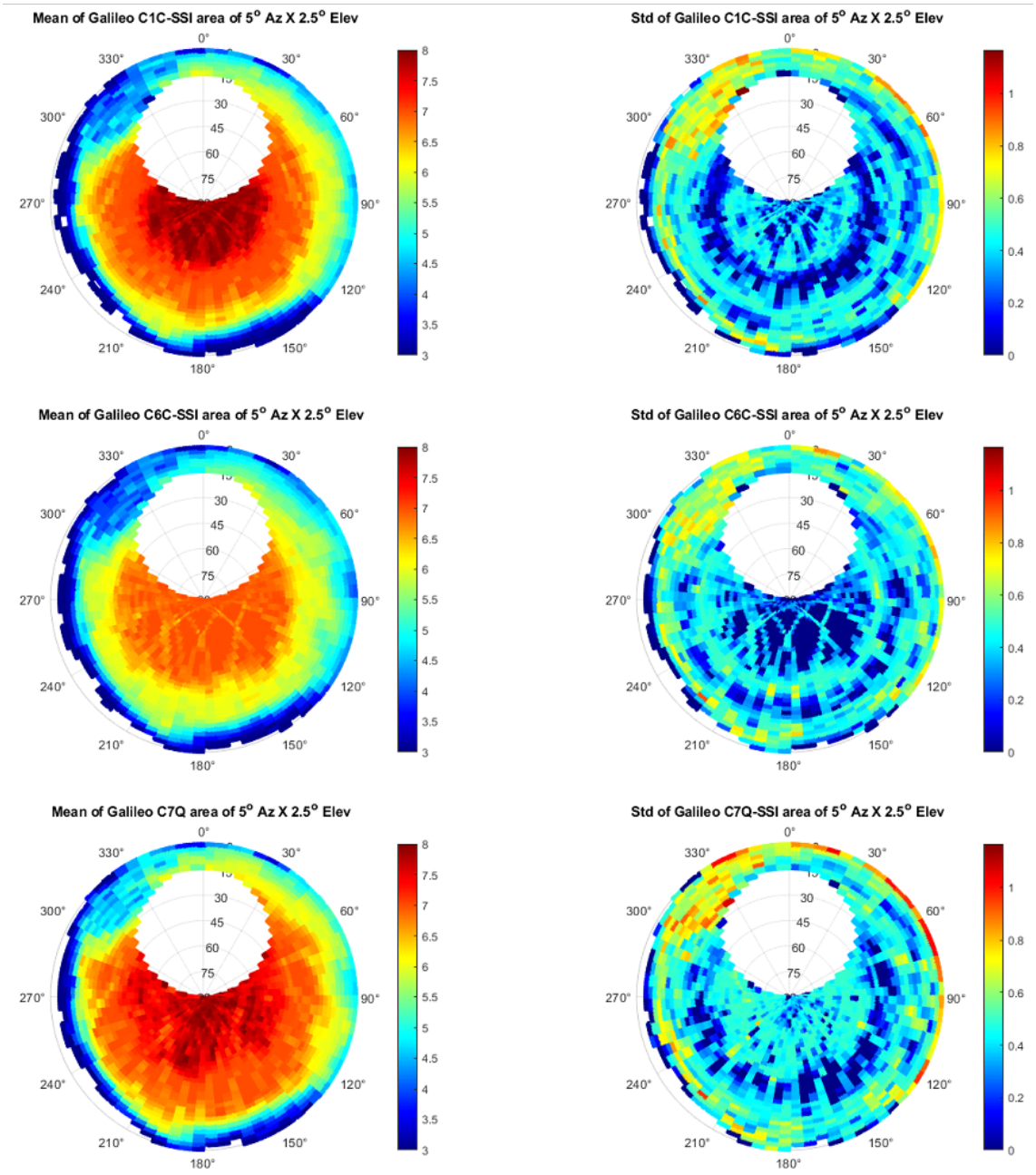

Figure 4.1: Sky plot displaying the mean (left) and standard deviation (right) of Galileo signal strength, combining all measurements simultaneously. Three different signals are depicted: C1C (1575.42 MHz frequency, top), C6C (1278.75 MHz frequency, middle), and CQ7 (1207.140 MHz frequency, bottom)

Regarding signal strength, C1C, with the highest frequency, exhibits the greatest strength but the least penetration ability. Notably, in the west, south, and southwest directions (approximately between azimuth 150^o to 300^o), low elevation signals are

obstructed by rocks and the building, resulting in a clear arc of empty cells in the mean SSI sky plots. In these directions there is a yellow arc in the standard deviation plot at an elevation of approximately 15^o, signifying high standard deviation. In other unobstructed directions, high standard deviation is observed mainly at low elevations between 0^o to 2.5^o, possibly due to to ground reflection.

4.1.2 GPS's signal strength

The mean SSI grids of GPS signals C1C and C2L for each arm orientation are presented in the subsequent Figures, 4.2 and 4.3. Typically, the C2L signal exhibits lower strength and more empty cells in its skyplots (seen in Figure 4.3) owing to its limited availability across all GPS satellites. However, its newer nature, stability, and superior quality prompted its utilization. It's important to note that primarily GPS signals were used in each directional analysis due to their consistent ground track positioning, i.e., their fixed sky positions as observed from the receiver's standpoint.

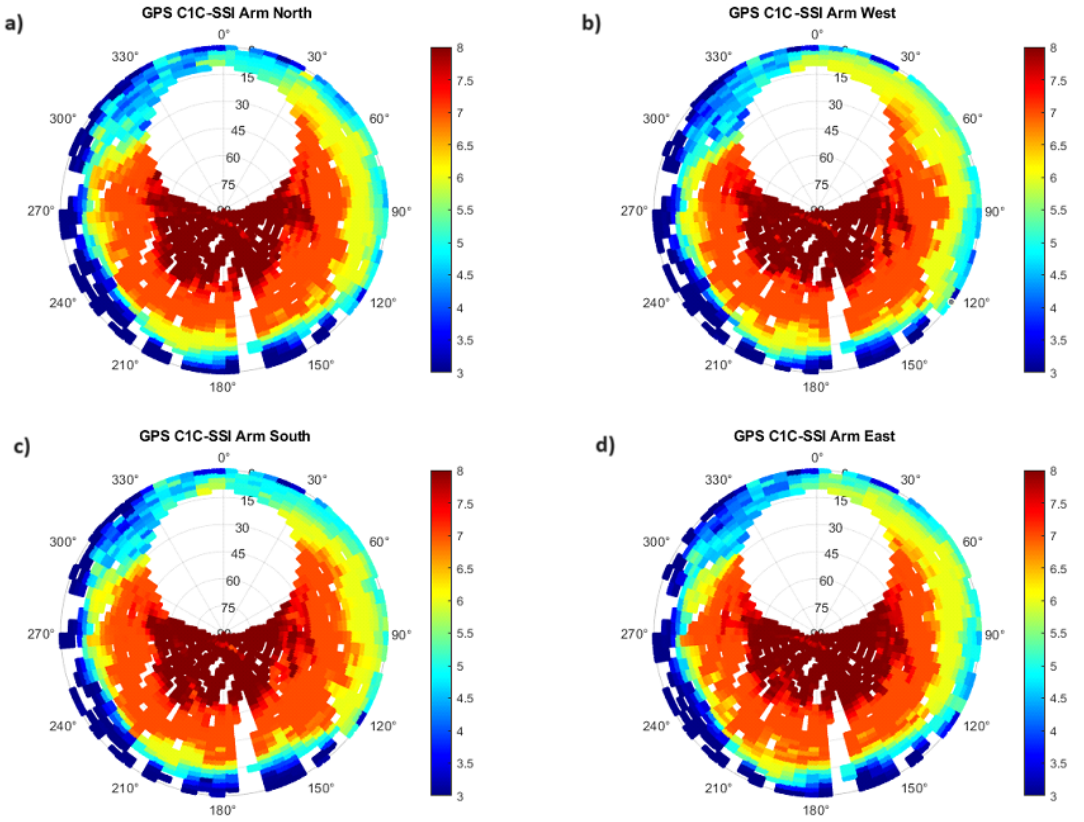

Figure 4.2: Sky plot of GPS color coded mean SSI of the signal C1C when the excavator's arm is pointing towards different directions: a)Arm pointing North, b)Arm pointing West, c)Arm pointing South and d)Arm pointing East

The orange and yellow areas in the GPS C1C and C2L skyplots vary noticeably based

on the excavator's arm orientation. After doing the digging scenario on September 9, the excavator's arm was returned to its initial north-facing direction. Comparisons were made between the mean SSI grid of GPS signals C1C and C2L on September 10 (regarded as an unknown direction,(refer to Figure 4.4) and the directional datasets. This comparison involved calculating the root mean square error (RMSE) and correlation coefficient. Results are depicted in Figures 4.5, 4.6, and 4.7. The Matlab function corrplot facilitated this comparison, showcasing scatterplots with least-squares reference lines and variable distribution histograms. The slope of each least-squares reference line is equal to the displayed correlation coefficient [36].

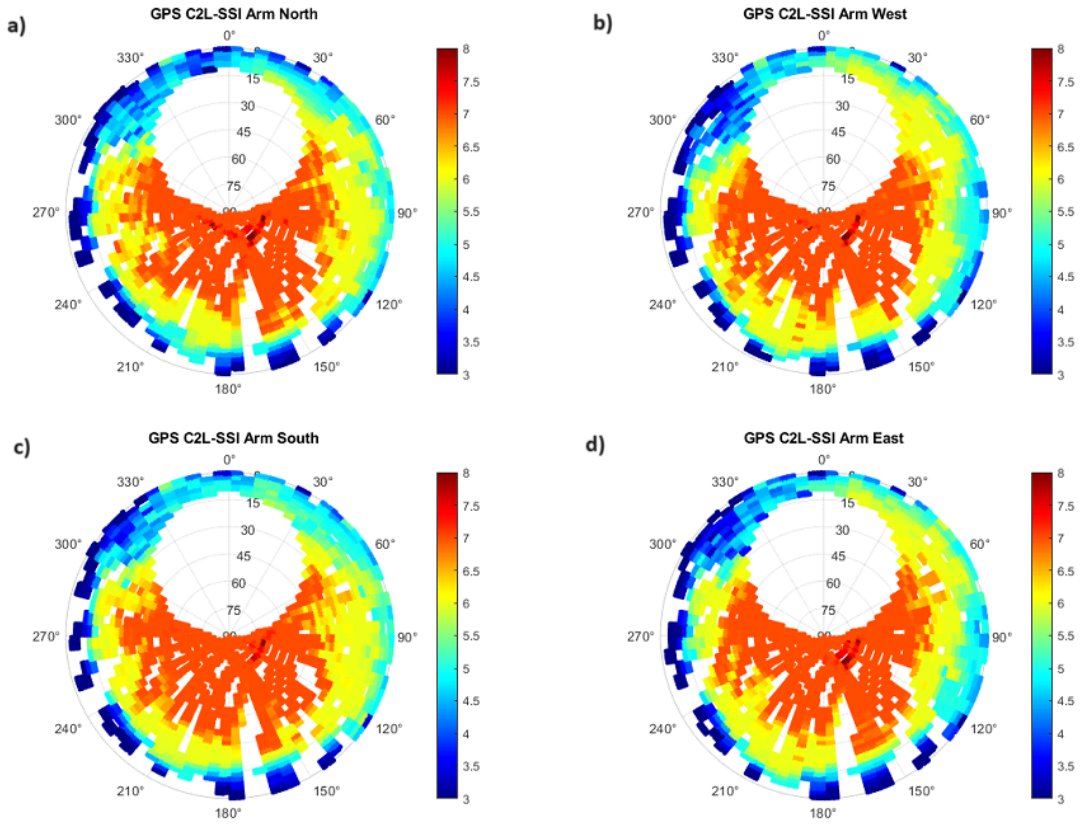

Figure 4.3: Sky plot of GPS color coded mean SSI of the signal C2L when the excavator's arm is pointing towards different directions: a)Arm pointing North, b)Arm pointing West, c)Arm pointing South and d)Arm pointing East

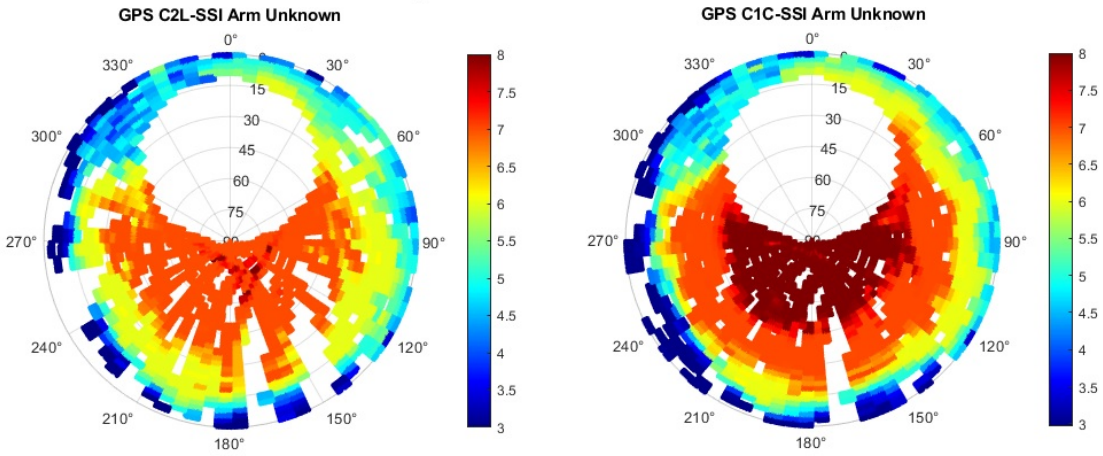

Figure 4.4: Sky plot of GPS color coded mean SSI of the signal C2L(left) and C1C(right) on September 10, Arm is pointing towards unknown direction

The RMSE values for both C1C and C2L are relatively low across all directions, with the north orientation displaying the lowest RMSE. Please note that whenever the north direction displays the lowest value in the RMSE test, it is highlighted in red on the RMSE figures. This highlighting indicates our anticipation that this direction aligns with the day of unknown direction. In the C1C correlation matrix, the unknown and north directions exhibit the highest correlation coefficient of 0.99, while strong correlation is evident among all directional data.

Receiver raw data indicated the excavator's arm orientation on September 10 probably faced north, unveiling a distinct relationship between the arm's orientation and the SSI skyplot values.

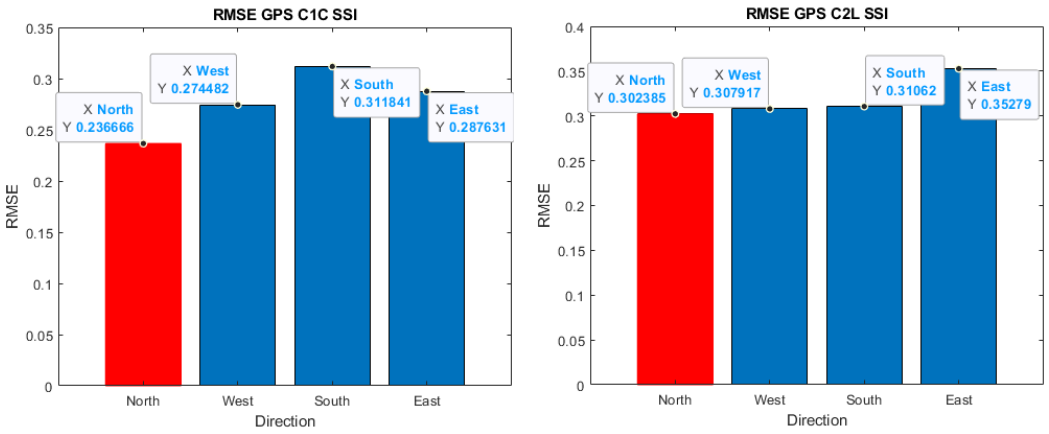

Figure 4.5: RMES values for SSI of both C1C(left) and C2L(right)

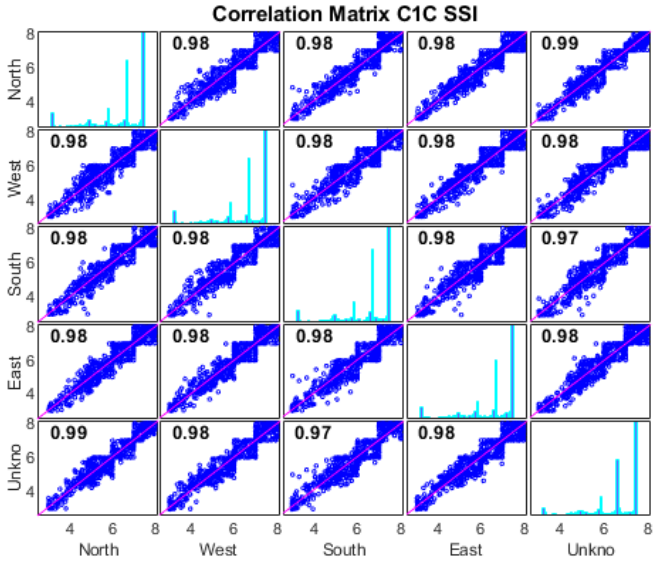

Figure 4.6: Correlation matrix for C1C SSI

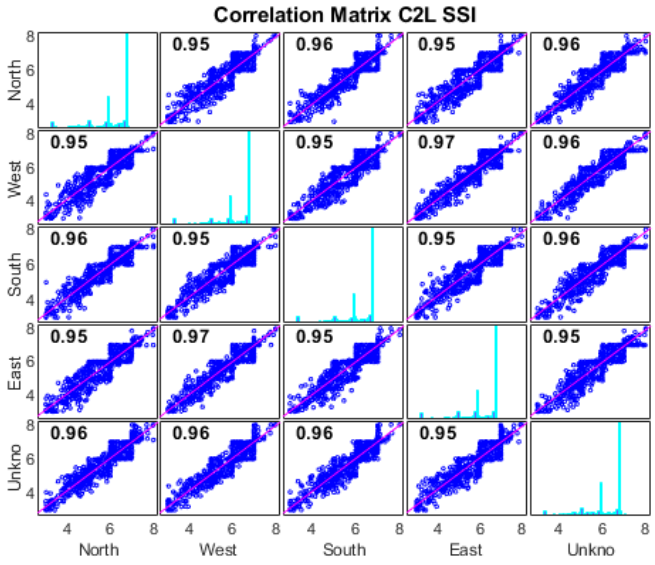

Figure 4.7: Correlation matrix for C2L SSI

4.2 Residuals

The analysis is continued by delving into the processed data. GipsyX in PPP mode were used to obtain post-fit carrier phase residuals, by forming the L3 sig-

nal ,Ionospheric-free combination. Equation 2.23 shows how L3 signal is formed and the procedure of obtaining residuals were described in the section 3.3.3.
Post-fit carrier phase residuals will simply be referred to as "residuals" hereafter. L1C and L2W signals, were used to produce L3. The selection of the L2W signal stems from its availability across all GPS satellites, although the newer signal L2L will be explored later. As mentioned earlier, the GipsyX software in PPP mode was utilized to process the data. The combination data from three systems—GPS, Glonass, and Galileo (GRE)—were initially processed with a 5-minute duration. Subsequently, the processing duration was reduced to 30 seconds in an attempt to move closer to real-time data processing.

4.2.1 Residuals vs Azimuth

Figures 4.8 and 4.9 illustrate all residuals and their moving average from all constellations plotted against azimuth. The range where the mean value demonstrates the least instability spans between azimuth 300^o and 350^o—an area notably influenced by the presence of a tree. All figures (4.8, 4.9, 4.10, and 4.11) include all residuals, including outliers. However, a specific threshold (set at 25 cm) has been applied, removing observations with residuals beyond this value from the position estimation process. Consequently, fewer data points are available between azimuth 300^o and 350^o, and many of these observations don't contribute to the final position estimation. Generally, mean residual values oscillate between -2 mm and 2 mm across most azimuths. Another direction displaying some instability in mean residuals lies between azimuth 0^o and 50^o, this is due to the fact that observations in this direction obtained from low-elevation satellites (less than 30^o in elevation).

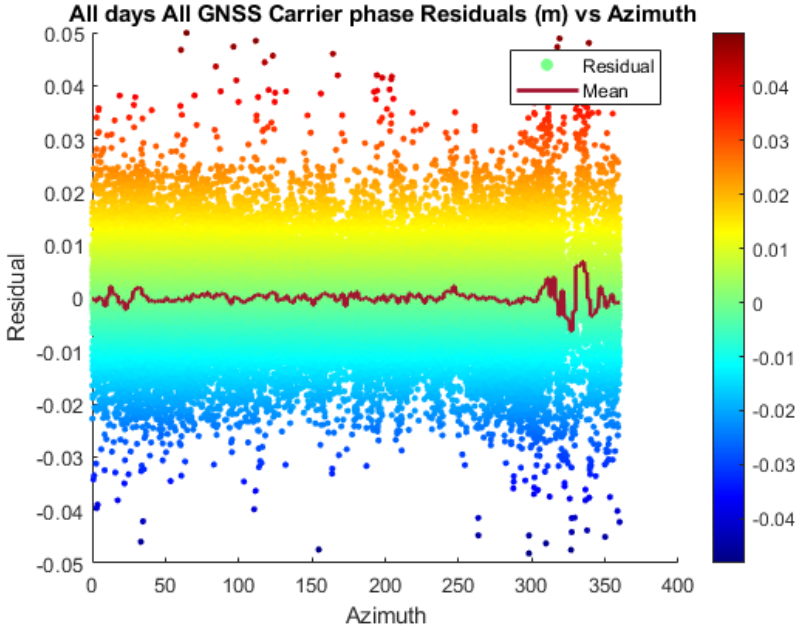

Figure 4.8: Residuals (m) vs Azimuth

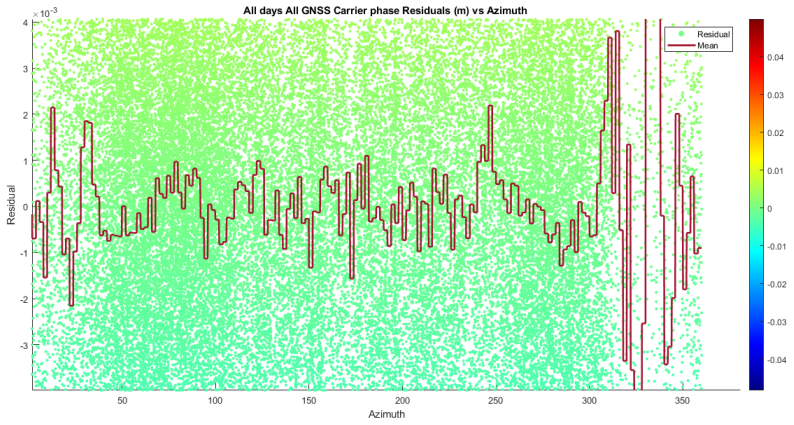

Figure 4.9: Residuals (m) vs Azimuth zoomed version

4.2.2 Residuals vs Elevation

The residuals in Figures 4.10 and 4.11 depict observations across all days and directions with zero cutoff angle, plotted against elevation. Notably, signals from elevations below 30^o showcase higher residuals. Observations between 0^o to 5^o exhibit a markedly strong negative mean residual but the number of observations at these low elevation angles is insufficient to draw any conclusion. Another significant observation emerges in the form of a peak in mean residuals between elevations of 60^o to 80^o, where the mean residual curve displays a concave pattern. Figure 4.11 provides a clearer view of this concavity. This elevation-related peak in residuals might be attributed to reflections originating from the excavator's body itself.

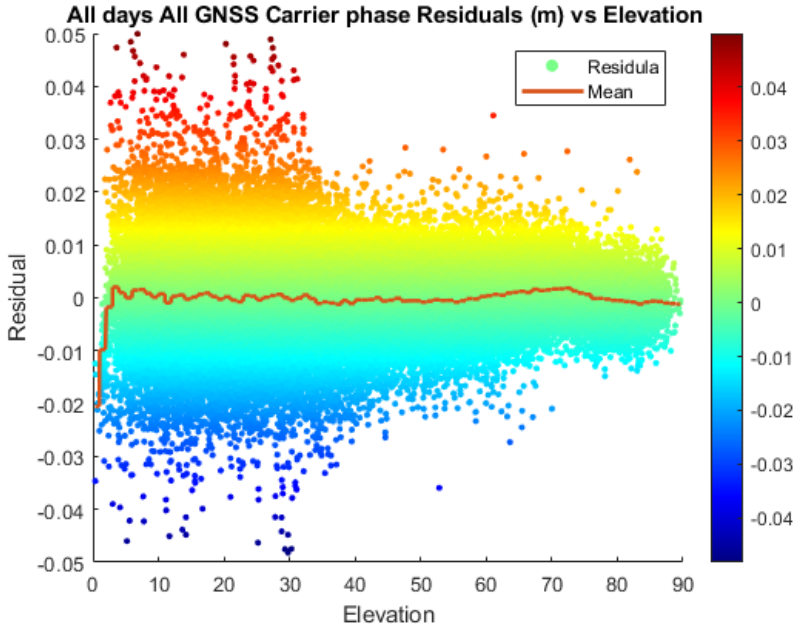

Figure 4.10: Residuals (m) vs Elevation

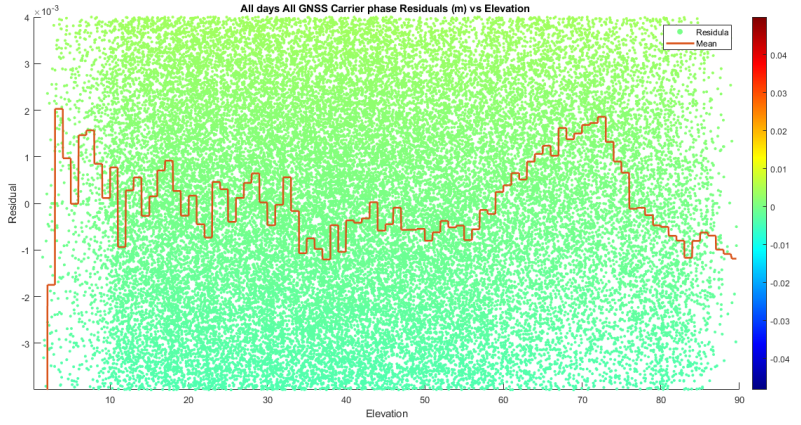

Figure 4.11: Residuals (m) vs Elevation zoomed version

4.2.3 Directional analysis

The upcoming Figures (4.12, 4.13 , 4.14, and 4.15) display the skyplots of GPS residuals for each direction. On the left side, a 0^o cutoff angle is employed, while the right side features a 10^o cutoff angle. Notably, utilizing a 10^o cutoff angle reduces the overall fluctuation in residuals across the entire skyplot.

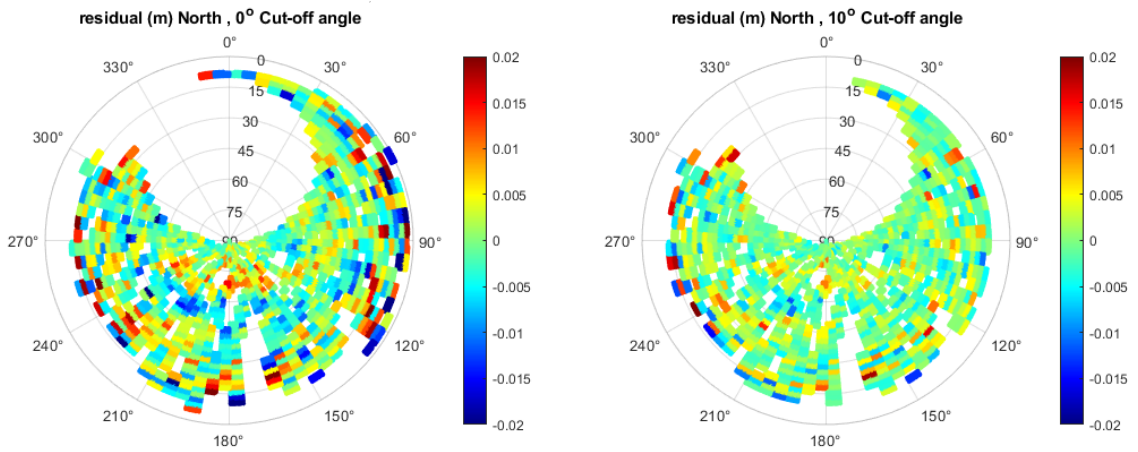

Figure 4.12: Sky plot of GPS color coded carrier phase residuals with 0^o cut-off(left) and with 10^o cut-off(right) , Arm is pointing towards North.

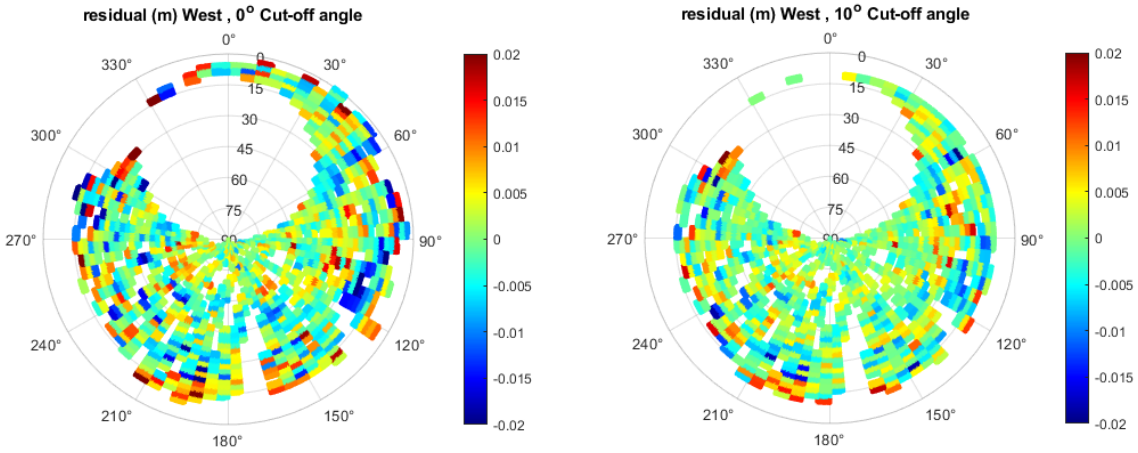

Figure 4.13: Sky plot of GPS color coded carrier phase residuals with 0^o cut-off(left) and with 10^o cut-off(right) , Arm is pointing towards West.

A comparative examination, like to the SSI analysis for each orientation, is performed to investigate any association between the residuals and the excavator's arm orientation. Once again, RMSE and correlation for each orientation with the residuals of 10th September (selected as the unknown orientation) are utilized. Note that as before whenever the north direction displays the lowest value in the RMSE test, it is highlighted in red on the RMSE figures.

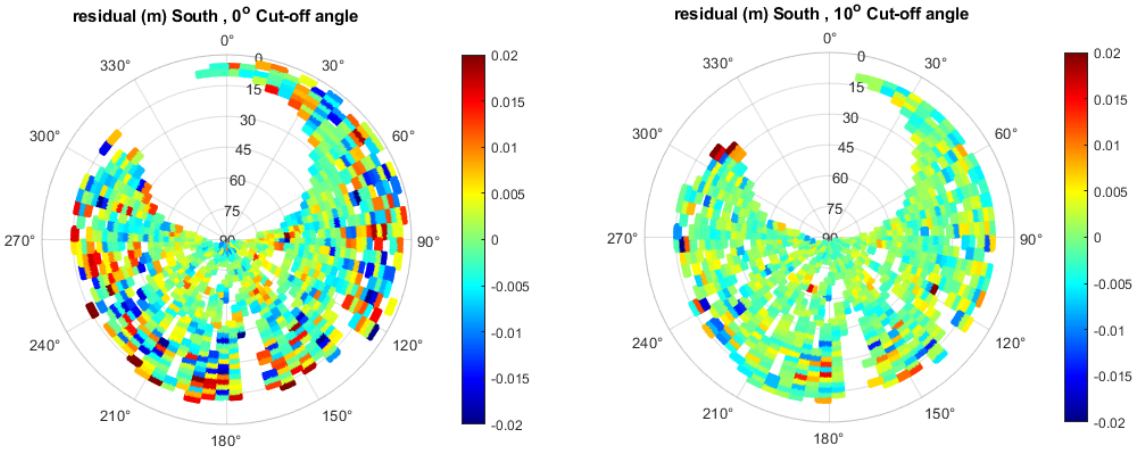

Figure 4.14: ky plot of GPS color coded carrier phase residuals with 0^o cut-off(left) and with 10^o cut-off(right) , Arm is pointing towards South.

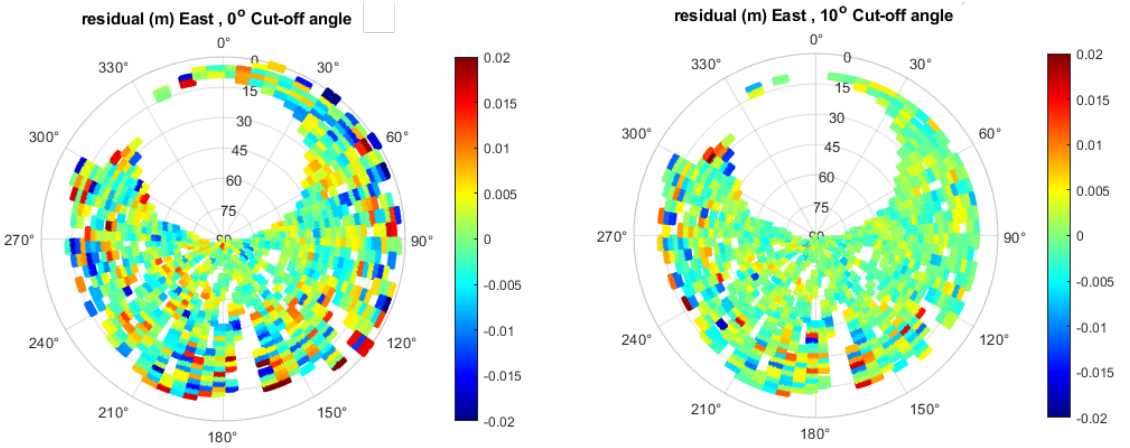

Figure 4.15: ky plot of GPS color coded carrier phase residuals with 0^o cut-off(left) and with 10^o cut-off(right) , Arm is pointing towards East.

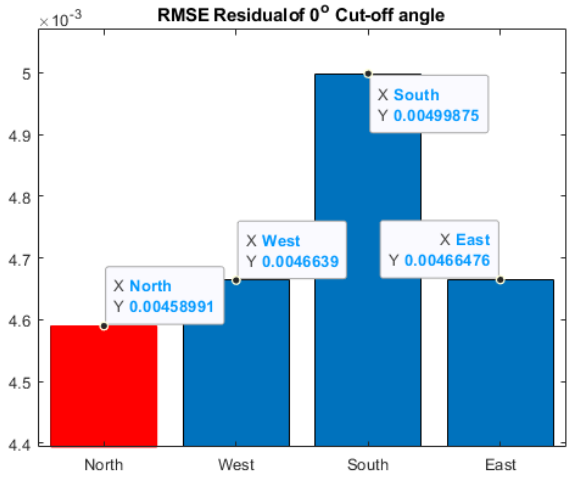

Figure 4.16: RMSE values for GPS Residuals with 0^o cut-off

Figure 4.16 illustrates RMSE for residuals with a 0^o cutoff angle, revealing the lowest RMSE for the North and the highest for the South. Figure 4.17 demonstrates RMSE for residuals with a 10^o cutoff angle, showcasing the North and East with the lowest RMSE, while slightly lower in the East. Overall, the RMSE values remain remarkably low. This is expected given that the surrounding environment of the antenna is not changing a lot although some variation caused by rotating the excavator's arm and this also cause some displacement of the antenna.

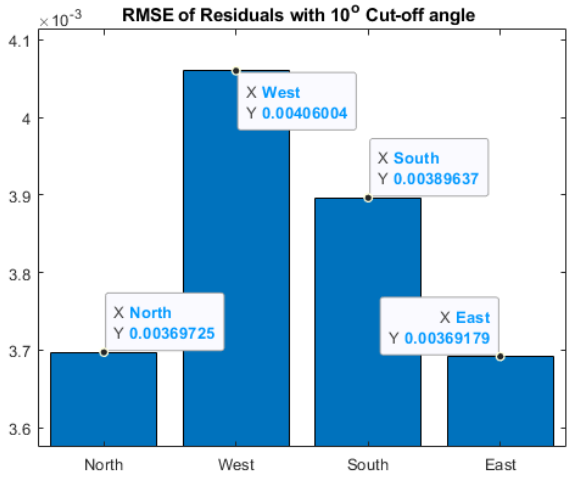

Figure 4.17: RMSE values for GPS Residuals with 10^o cut-off

Figures 4.18 and 4.19 present correlation coefficients of various arm orientations for 0^o and 10^o cutoff angle residuals, respectively. Unlike the SSIs, the correlation coefficients for residuals are notably lower. With a 0^o cutoff angle, the West direction

shows the highest correlation with the unknown direction, followed by North and South. For a 10^o cutoff angle, both North and East exhibit the highest correlation with the unknown.

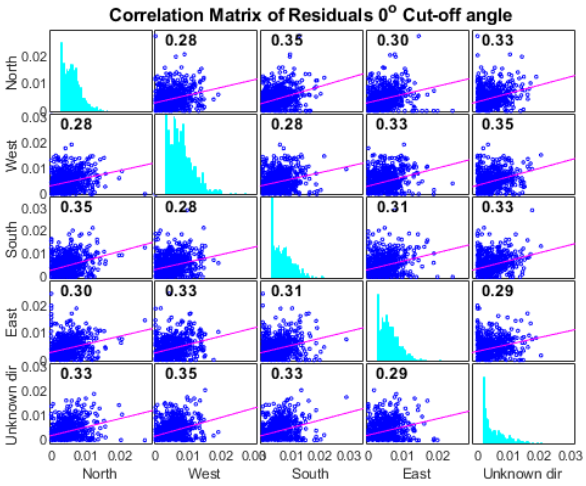

Figure 4.18: Correlation matrix for GPS Residuals with 0^o cut-off

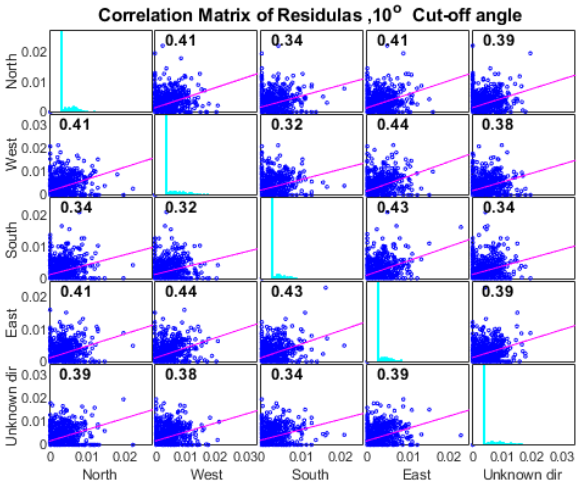

Figure 4.19: Correlation matrix for GPS Residuals with 10^o cut-off

In an attempt to investigate further the results, the ionospheric-free combination involving L2L was also produced, despite its limited availability across GPS satellites. Although the skyplots for these residuals closely resemble previous ones, only the results for RMSE and correlation are presented.

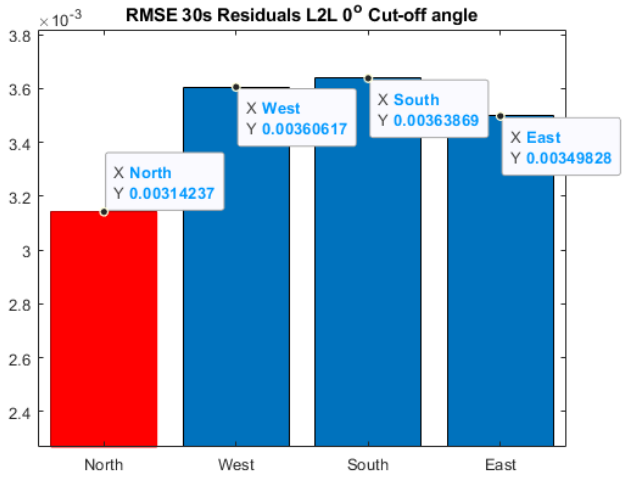

Figure 4.20: RMSE values for GPS Residuals when the new L2L signal is used with 0^o cut-off

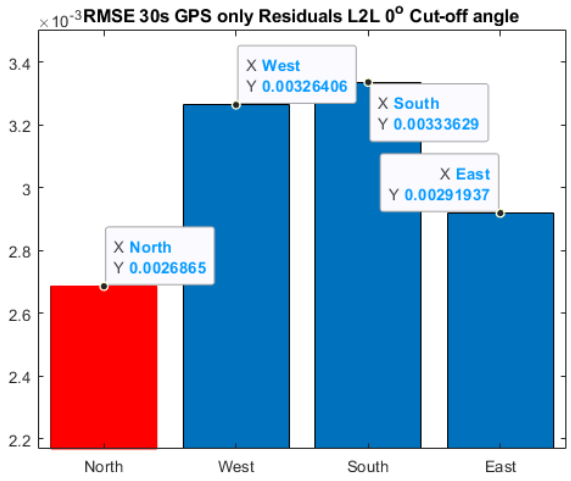

Figure 4.21: RMSE values for GPS Residuals when the new L2L signal and only GPS observations are used with 0^o cut-off

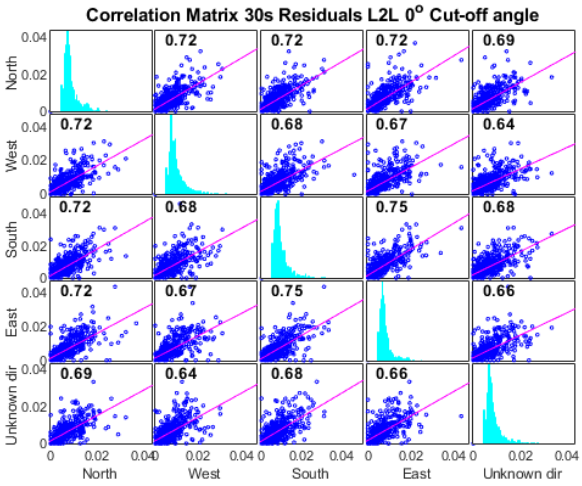

Figure 4.22: Correlation matrix for GPS Residuals when the new L2L signal is used with 0^o cut-off

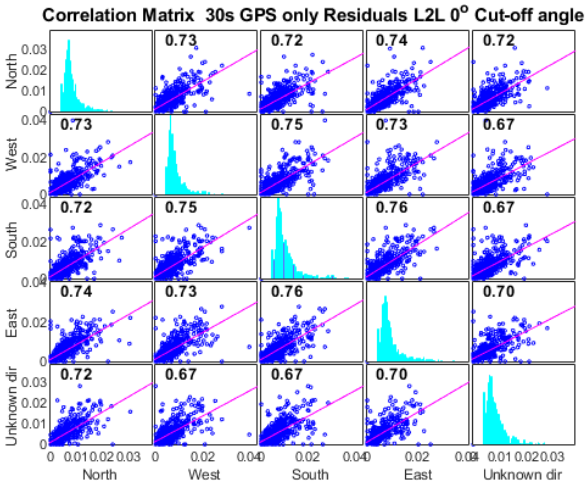

Figure 4.23: Correlation matrix for GPS Residuals when the new L2L signal and only GPS observations are used with 0^o cut-off

When the L2L signal is utilized, the correlations between residuals notably improve. The unknown direction appears to have the highest correlation with the North direction. Similarly, the North direction exhibits the lowest RMSE when employing the L2L signal. Refer to Figures 4.20, 4.21, 4.22, and 4.23 for a detailed depiction of these results. Note that in Figures 4.21 and4.23, only the GPS data was utilized for processing.

4.3 Position estimation

Figure 4.24: Estimation of each component(XYZ) of 3D position and their uncertainties, X at the top , Y in the middle and Z at the bottom

Position estimations have been done both with and without the signal L2L, utilizing both 5-minute and 30-second processing intervals. To ensure more accurate estimations, a 5^o cutoff angle was employed in all estimations to eliminate noisy data. Figure 4.24 illustrates the estimations for each component (XYZ) of the 3D position. It's important to note that these components are presented in the International Terrestrial Reference Frame (ITRF), with its origin at Earth's geocenter and rotating along with the Earth. The mean has been removed from each component to facilitate observation of the change caused by the excavator's arm rotation.

On the right side of Figure 4.24, position estimations using a 30-second processing time with the new L2L signal are displayed, while on the left side, estimations derived from 5-minute processing with the old C2W signal are presented. Estimations based on the L2L signal exhibit greater stability, showing minimal errors in static mode, approximately around 1 mm. Conversely, using the old C2W signal for 5-minute positioning results in higher uncertainties, roughly ranging from 2-3 cm for each component, with the Z component demonstrating the most noise. Interestingly, the 5-minute position estimations appear less sensitive to the digging scenario conducted on September 9th compared to the 30-second data. Digging causes an increase up to 1-2 cm in uncertainty across all components throughout the entire day on September 9th.

Three Figures, 4.25, 4.26, and 4.27, depict the 2D position estimations of the receiver antenna. Notably, when processing is conducted using L2L, the final position estimations exhibit significantly greater stability and repeatability. Upon closer inspection of Figures 4.26 and 4.27, it's apparent that the final position of the antenna on September 10th (depicted by light blue dots) does not precisely align with the orientation when the arm was pointed north (illustrated by dark blue and red dots on September 4th and part of September 5th). However, it does remain closest to the North direction. Two potential scenarios arise from this observation: The first possibility is that the excavator's operator did not precisely align the arm towards the North. Alternatively, during the digging scenario, the entire excavator might have shifted slightly, thereby altering the final position of the antenna. The former scenario seems more probable, considering the 30-second position estimations demonstrate the antenna's movement along the circumference of an imaginary circle, with the movement concluding on this circumference.

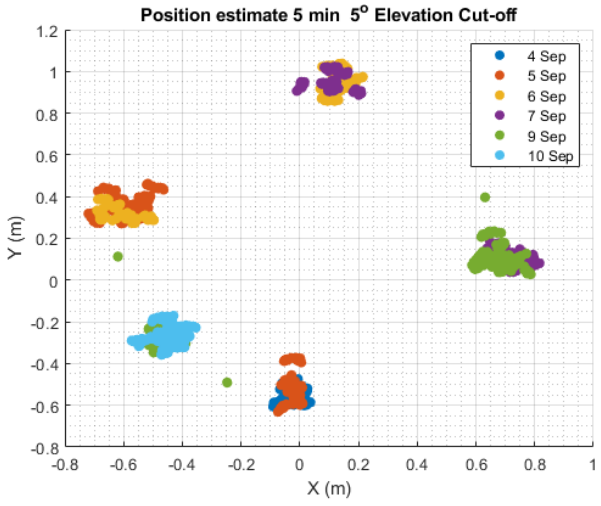

Figure 4.25: 2D position estimation with 5 minutes processing time

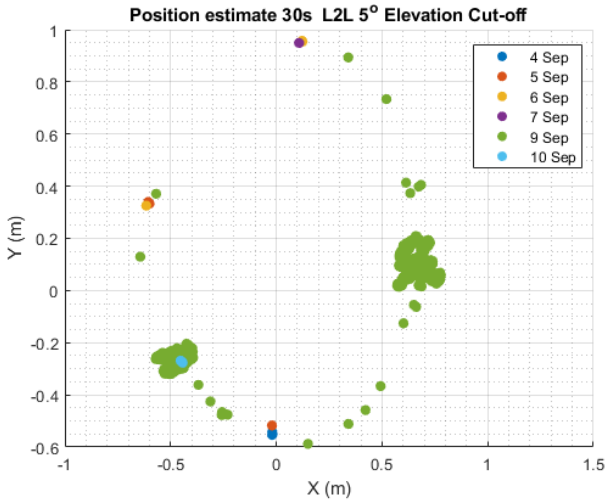

Figure 4.26: 2D position estimation with the new signal L2L and with 30 seconds processing time

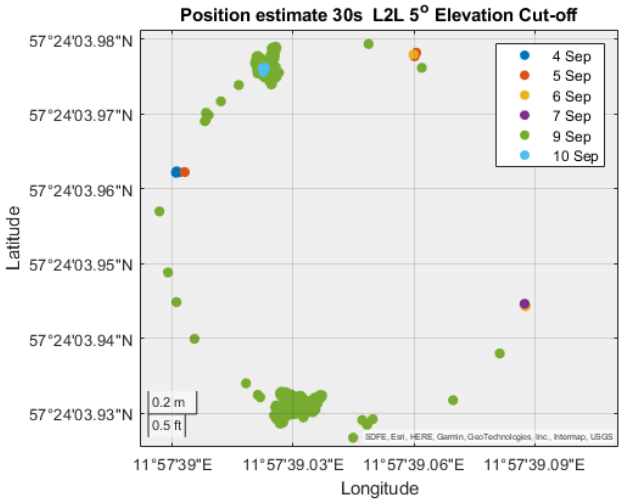

Figure 4.27: 2D position estimation with the new signal L2L and with 30 seconds processing time , given in latitude and longitude

5
Conclusion

The analysis of GPS SSI from Rinex files and GPS post-fit residuals revealed a systematic effect related to the orientation of the excavator's arm. The detectable influence in SSI implies the potential for predicting the arm's orientation even before data processing. Utilizing residuals allows modeling of the effects and errors linked to different arm orientations, presenting an avenue for enhanced accuracy in data processing.
Optimal performance was attained using the L2L signal, showcasing higher correlations among residuals with the same arm orientations. Enhanced repeatability in position estimations was evident with this signal. This indicates that employing both RMSE values and correlation coefficients concurrently could serve as an effective means to forecast the arm's orientation.
Carrier phase residuals provided insight into both the excavator's surface effects and the arm's orientation impact on the signal. They, alongside SSIs, elucidate environmental influences such as shadowing, diffraction from trees and buildings, and multipath effects caused by ground reflection.
The elevation angle analysis of all residuals highlighted two distinct effects: a negative mean between 0^o to 5^o elevation angles and a peak and concave behavior between 60^o to 80^o elevation angles. The latter is presumed to stem from reflections off the excavator's surface. The number of observations at low elevation angles between 0^o to 5^o is insufficient to draw any conclusion.

Future work: could involve expanding observations for each direction into several days or a week, enabling easier modeling of forthcoming effects in residuals. Considering Galileo's ground track in longer observation time covers the entire sky, analyzing its residuals could provide a comprehensive understanding of arm orientation effects. Furthermore, modeling effects on residuals for individual GPS satellites separately, albeit unexplored due to time constraints, could be a valuable avenue for deeper analysis. When the modelling of the effects and errors linked to different arm orientations is done the results can be used to improve position estimation in the similar and even more complex areas with more objects contributing to reflection, causing multipath effect or blockage to the signals. When the modelling of the effects and errors linked to body of the excavator and different arm orientations is completed, this models can be applied to real time positioning system in order to improve its performance.

Bibliography

[1] Rozhok, Andrii. Orientation and navigation in vertebrates. Berlin: Springer, 2008.

[2] Misra, Pratap, and Per Enge. "Global position systems: Signals, measurements and performance." Ganga-Jamuna Press, (2006).

[3] Sanz, J., J. M. Juan, and M. Hernández-Pajares. "GNSS Data Processing, Volume I: Fundamentals and Algorithms." (2013). available: https://gssc.esa.int/navipedia/GNSS_Book/ESA_GNSS-Book_TM-23_Vol_I.pdf

[4] Diamantidis, Periklis-Konstantinos. Exploring Strategies for the Combination of Multiple Space-Geodetic Techniques. Diss. Chalmers Tekniska Hogskola (Sweden), 2020.

[5] Rozhok, Andrii. Orientation and navigation in vertebrates. Berlin: Springer, 2008.

[6] Bacci, Giacomo, et al. "Satellite-Based Navigation Systems." Satellite and Terrestrial Radio Positioning Techniques. Academic Press, 2012. 25-74.

[7] Moore, Terry. "Understanding GPS/GNSS: Principles and Applications , Edited by ED Kaplan and CJ Hegarty Artech House, 16 Sussex Street, London, SW1V 4RW, UK. 2017. xxi; 993pp. Illustrated£ 155 ISBN 978-1-63081-058-0." The Aeronautical Journal 123.1266 (2019): 1323-1323.

[8] Kaplan, Elliott D., and Christopher Hegarty, eds. Understanding GPS/GNSS: principles and applications. Artech house, 2017.

[9] Saakian, Artem. Radio wave propagation fundamentals. Artech House, 2020.

[10] SCHROCK, GAVIN. "GUIDE, ASSIST, AUTOMATE: Even as Sensors and Systems for Construction Automation Evolve, GNSS Remains the Key Foundational Element for Most Applications." GPS World, vol. 34, no. 3, Mar. 2023, pp. 26–33. Avalable: EBSCOhost, search.ebscohost.com/login.aspx?direct=true&AuthType=sso&db=bsu&AN=162462287&authtype=sso&custid=s3911979&site=ehost-live&scope=site.

[11] Teunissen, Peter JG, and Alfred Kleusberg, eds. GPS for Geodesy. Springer Science & Business Media, 2012.

[12] The Image is Available at https://www.navcen.uscg.gov/gps-constellation

[13] Najibi, Nasser, and Shuanggen Jin. "Physical reflectivity and polarization characteristics for snow and ice-covered surfaces interacting with GPS signals." Remote Sensing 5.8 (2013): 4006-4030.

[14] Hofmann-Wellenhof, Bernhard, Herbert Lichtenegger, and James Collins. Global positioning system: theory and practice. Springer Science & Business Media, 2012.

[15] Hofmann-Wellenhof, Bernhard, Herbert Lichtenegger, and Elmar Wasle. GNSS–global navigation satellite systems: GPS, GLONASS, Galileo, and more. Springer Science and Business Media, 2007.

[16] Leick, Alfred, Lev Rapoport, and Dmitry Tatarnikov. GPS satellite surveying. John Wiley & Sons, 2015.

[17] Ávila Rodríguez, J. "GPS Signal Plan.[Online]Navipedia, European Space Agency. Available at: http://www. navipedia. net/index. php." (2011).

[18] Ogaja, Clement A. "Applied GPS for engineers and project managers." American Society of Civil Engineers, 2011.

[19] Gebre-Egziabher, Demoz, and Scott Gleason. GNSS applications and methods. Artech House, 2009.

[20] Robinson, Enders A., and Dean Clark. Basic geophysics. Tulsa: Society of Exploration Geophysicists, 2017.

[21] Kindervatter, Timothy H., and Fernando L. Teixeira. Tropospheric and Ionospheric Effects on Global Navigation Satellite Systems. John Wiley & Sons, 2022.

[22] Smith, Ernest K., and Stanley Weintraub. "The constants in the equation for atmospheric refractive index at radio frequencies." Proceedings of the IRE 41.8 (1953): 1035-1037.

[23] Parkinson, B., J. Spilker, and P. Enge. "Global positioning system, vols I and II, Theory and Applications." American Institute of Aeronautics, Reston (1996).

[24] Romero, Ignacio. "The receiver independent exchange format version 3.05." International GNSS Service Files, https://files. igs. org/pub/data/format/rinex305. pdf (2020).

[25] Luo, Xiaoguang. GPS stochastic modelling: signal quality measures and ARMA processes. Springer Science & Business Media, 2013.

[26] Xu, Guochang, and Yan Xu. GPS. Springer-Verlag Berlin Heidelberg, 2007.

[27] Teunissen, Peter JG, and Oliver Montenbruck, eds. Springer handbook of global navigation satellite systems. Vol. 10. Cham, Switzerland: Springer International Publishing, 2017.

[28] Hunegnaw, Addisu, and Felix Norman Teferle. "Evaluation of the Multipath Environment Using Electromagnetic-Absorbing Materials at Continuous GNSS Stations." Sensors 22.9 (2022): 3384.

[29] , Günter, and Günter Seeber. Satellite Geodesy : Foundations, Methods, and Applications, De Gruyter, Inc., 2003. ProQuest Ebook Central, https://ebookcentral.proquest.com/lib/chalmers/detail.action?docID=325660.

[30] , Shahid, Jonathan Rodriguez, and Linglong Dai. MmWave massive MIMO: a paradigm for 5G. Academic Press, 2016.

[31] Zimmermann, Florian, et al. "GPS multipath analysis using fresnel zones." Sensors 19.1 (2018): 25.

[32] Hannah, Bruce M. Modelling and simulation of GPS multipath propagation. Diss. Queensland University of Technology, 2001.

[33] National Aeronautics and Space Administration, "RINEX Version 3 data", Nov. 29, 2018. Accessed: Dec. 22, 2020. [Online]. Avalable: `https://cddis.nasa.gov/Data_and_Derived_Products/GNSS/RINEX_Version_3.html`

[34] Abraha, K. E., et al. "SWEPOS data quality monitoring–GNSS Signal Disturbances Detection System." (2021).
[35] Hunegnaw, Addisu, et al. "On the Impact of GPS Multipath Correction Maps and Post-Fit Residuals on Slant Wet Delays for Tracking Severe Weather Events." Atmosphere 14.2 (2023): 219.
[36] https://se.mathworks.com/help/econ/corrplot.html

DEPARTMENT OF SOME SUBJECT OR TECHNOLOGY
CHALMERS UNIVERSITY OF TECHNOLOGY
Gothenburg, Sweden
www.chalmers.se

CHALMERS
UNIVERSITY OF TECHNOLOGY